Environmental Modeling & Assessment
https://doi.org/10.1007/s10666-020-09746-2

Assessing the Vulnerability of a Deltaic Environment due to Climate Change Impact on Surface and Coastal Waters: The Case of Nestos River (Greece)

Charalampos Skoulikaris[1] · Christos Makris[2] · Margarita Katirtzidou[2] · Vasilios Baltikas[2] · Yannis Krestenitis[2]

Received: 30 May 2020 / Accepted: 18 December 2020

Abstract
In deltaic areas, riverine and coastal waters interact; hence, these highly dynamic environments are particularly sensitive to climate change. This adds to existing anthropogenic pressures from irrigated agriculture, industrial infrastructure, urbanization, and touristic activities. The paper investigates the estimated future variations in the dynamics of surface and coastal water resources at a Mediterranean deltaic environment for the twenty-first century. Therefore, an Integrated Deltaic Risk Index (IDRI) is proposed as a vulnerability assessment tool to identify climate change impact (CCI) on the study area. For this purpose, three regional climate models (RCM) are used with representative concentration pathways (RCPs) 4.5 and 8.5 for short-term (2021–2050) and long-term (2071–2100) future periods. Extensive numerical modeling of river hydrology, storm surges, coastal inundation, water scarcity, and heat stress on irrigated agriculture is combined with available atmospheric data to estimate CCI on the Nestos river delta (Greece). The IDRI integrates modeling results about (i) freshwater availability covering agricultural demands for three water consumption scenarios, i.e., a reference (REF), a climate change (CC), and an extended irrigation (EXT) scenario, combining river discharges and hydropower dam operation; (ii) inundated coastal areas due to storm surges; and (iii) heat stress on cultivated crops. Sustainable practices on irrigated agriculture and established river basin management plans are also considered for the water demands under combinatory scenarios. The differentiations of model outputs driven by various RCM/RCP combinations are investigated. Increased deltaic vulnerability is found under the RCP8.5 scenario especially for the long-term future period. The projected IDRI demonstrates the need for integrated water resources management when compared with risk indexing of individual water processes in the study area.

Keywords Vulnerability assessment · Climate change impact · River delta · Coastal zone · Integrated modeling · Risk index

Abbreviations

AR5	5th Assessment Report
CC	Water consumption scenario for climate change
CCI	Climate change impact
CFR	Coastal Flood Risk Index
CMCC	Climate Model CMCC-CCLM4-8-19 v.1
CNRM	Climate Model CNRM-ALADIN52 v.1
CVI	Coastal Vulnerability Index
EXT	Water consumption scenario for EXTended irrigation
GUF	Climate Model GUF-CCLM-NEMO4-8-18 v.1
HiReSS	High-Resolution Storm Surge model
HPP	Hydropower plant
HRP	Hit-rate-of-percentiles
HSRI	Heat Stress Risk Index
HT	High temperature
HTP	High temperature probability
IDRI	Integrated Deltaic Risk Index
IPCC	Intergovernmental Panel on Climate Change
LTF	Long-term future
MeCSS	Mediterranean Climatic Storm Surge model

✉ Charalampos Skoulikaris
hskoulik@civil.auth.gr

[1] UNESCO, Chair INWEB, Aristotle University of Thessaloniki, 54124 Thessaloniki, Greece

[2] Division of Hydraulics and Environmental Engineering, School of Civil Engineering, Aristotle University of Thessaloniki, 54124 Thessaloniki, Greece

Published online: 28 January 2021

MED-CORDEX	MEDiterranean COordinated Regional climate Downscaling EXperiment
MODSUR	MODelisation du SURface model
MSL	Mean seal Level
RCM	Regional climate model
RCP	Representative concentration pathway
REF	Reference water consumption scenario
RP	Reference period
SLP	Sea level pressure
SSH	Sea surface height
SSI	Storm Surge Index
STF	Short-term future
WCS	Water consumption scenario
WEAP	Water evaluation and planning model
WFD	Water Framework Directive

1 Introduction

Facts and figures demonstrate the socioeconomic and ecologic importance of the river deltas. Although deltaic regions cover approximately 1% of land area globally, they host more than half a billion people, i.e., 7% of the world population [1]. Thus, they stand out as very important areas of human activities, such as intensified agriculture and industrial production [2]. For example, the Pearl River Delta occupies almost 0.5% of the Chinese mainland; however, it accounts for 10% of the country's gross domestic product [3]. In terms of their ecological value, the environmental services of deltaic areas are extensively demonstrated in relevant literature [4, 5]. Based on the Convention of Wetlands database[1] (Ramsar), more than 66% of environmentally protected areas are located below 500 m altitude, indicating that a large part of protected wetlands is located in deltaic areas and coastal zones. Similarly, the European Union (EU) network of nature protection areas, namely Natura 2000,[2] includes the deltaic areas of almost all EU rivers. Greece is a characteristic example, where all the main rivers' deltas are Natura 2000 environmentally protected areas, i.e., designated for conservation of the most seriously threatened habitats, species, and birds. The complex interactions between land-based fluvial flows and coastal water processes render deltas as particularly interesting areas of research [6].

The Mediterranean basin is considered a hotspot in terms of climate change projections [7, 8]. Models and scenarios of the latest Intergovernmental Panel on Climate Change (IPCC) 5th Assessment Report (AR5) [9] demonstrate that the basin's future climate will be characterized by monthly net rainfall decrease during winter and potential evapotranspiration increase during summer due to global warming. Consequently, climate change is expected to affect surface fresh waters' availability, especially in conjunction with manmade pressures, such as the overexploitation of aquatic resources for the coverage of increased water demands for irrigation and water supply purposes [10]. The latter is anticipated to directly impact the environmental services of areas where different interests on water uses are met [11]. Drought phenomena will also exert pressure on the deltaic environment, especially on littoral agricultural land [12–14]. Focusing on deltaic agriculture, the raising frequency, duration, and intensity of droughts will seriously affect the crop development and yield [15]. High temperature (HT) over predefined thermal thresholds is a significant environmental stress that affects plant growth, metabolism, agricultural productivity, and crop yield [16–18], with HT impacts to be exacerbated due to the projected temperature increase [19]. Thus, proper management of water availability and irrigation demands as well as efficient irrigation practices are becoming essential for sustaining crop production [20–25] under climate change.

In regions where terrestrial waters meet coastal seawaters, the impact of climate change is expected to be more severe. The storm-induced sea level impacts on deltaic areas are thoroughly investigated in the literature [26–28], as well as the effects of climate change on extremes and mean conditions of storm surges on the Mediterranean coastal areas [29–37]. Kaniewski et al. [38], nevertheless, indicate that for the Mediterranean Sea in particular, research about climate-related storm impacts on flooding of deltaic areas is rather limited. Only recently, Paprotny et al. [39] presented an investigation of compound flood, i.e., storm surges and inland runoffs interactions, identification in pan-European level (yet not in the framework of future projections under climate change).

Vulnerability assessment, i.e., the process of identifying the problem (hazard), quantifying the problem (exposure) and assessing the impact rate, is a way to interpret the anthropogenic and natural pressures on the environment [40], a process that is also used in deltaic systems. The vulnerability index–based methods [41] combine several indicators into a single index, allowing an easy comparison between parameters and sectors. In the early 1990s, one of the first attempts to define a Coastal Vulnerability Index (CVI) was developed to investigate the sea level rise impact in terms of coastal inundation and erosion [42]. Since then, a significant number of vulnerability indices were formulated for specific case studies using various sources of data and integrating uncertainty [43–46]. Focusing on drought, various drought indexes have also been developed assessing the frequency, severity, duration, and spatial extent of droughts [47–49], with drought vulnerability being assessed in numerous case studies [50, 51] including irrigated agriculture [52, 53].

[1] https://rsis.ramsar.org/

[2] https://natura2000.eea.europa.eu/

This paper proposes the use of an Integrated Deltaic Risk Index (IDRI), combining high temperature stress on agriculture, lack of irrigation water through river runoff simulations, and inundated coastal areas, in order to identify the vulnerability of deltaic areas due to climate change impact (CCI). The input data fed to the IDRI are produced by advanced numerical models for catchment hydrology and river runoff, hydropower dam operation, agricultural irrigation, storm surges, and consequent coastal flooding simulations. The latter are implemented in long-term mode (covering the 1971–2100 period), under different climate change projection scenarios. In the proposed methodology, a reference water consumption scenario (termed REF, hereafter) based on the current irrigation patterns, but for climate change conditions, is indexed for the assessment of the vulnerability in the case study area. The same index is estimated for the case of escalating demands on irrigating water as derived from future climatic variables (climate change water consumption scenario; designated as CC, hereafter). The excess water volumes that are identified when sustainable agricultural patterns are adopted, i.e., in water consumption scenario CC, trigger the assessment of the same index when development plans, such as the extension of irrigation networks, are proposed (water consumption scenario for extended irrigation; abbreviated as EXT, hereafter). The proposed methodology is demonstrated to the Nestos river delta in Greece (see Sect. 2.1), where all the water uses are met with irrigated agriculture to be the larger water consumer.

All methodological approaches, implemented models, and integration of results via risk index assessment specifically for the case study's deltaic characteristics are presented in Sect. 2. Section 3 contains the storm surge, river hydrology, and water management models' validation. Section 4 presents all modeling and index estimation results related to climate change impact on vulnerable deltaic areas of the study region. A discussion of produced output comparing new findings with previous literature is attempted in Sect. 5, followed by the concluding remarks of the presented study in Sect. 6.

2 Methodology

The development of a conceptual modeling framework is proposed as the principal methodological approach; schematics of input data and modeling results' flow is presented in Fig. 1. Within it, locally important processes were simulated in the coastal zone and river delta, thereafter, to be indexed in an integrated risk assessment framework (see IDRI description in Sect. 2.6). Thus, the integration of four large-scale modeling components is carried out for the selected case study covering the following levels of implementation for:

a) The atmosphere over the deltaic area by climatic forcing input (e.g., winds, atmospheric pressure, precipitation, temperature) from available databases (MED-CORDEX) for historical and future climate change scenarios (see Sect. 2.2)
b) The coastal zone in the vicinity of the delta by the simulation of storm surges in the maritime area (MeCSS model) and the estimation of consequent overland inundation extends (CoastFLOOD module) for extreme events (see Sect. 2.3.1)
c) The land of the upper delta by hydrologic simulations (MODSUR model; see Sect. 2.3.2) of a transboundary river catchment, including the simulation of the basin's hydropower plants (WEAP hydropower simulation module, see also Sect. 2.3.2) to estimate the water demand and supply balance (WEAP model; see Sect. 2.4) in different management periods of climate projections and under three different water consumption scenarios (WCS)
d) The agricultural areas in the delta by simulating the irrigation demands on water and heat stress assessment (by climatic forcing of level a) per crop (see Sect. 2.5)

All the above and their outputs are conceptually integrated into the development of an index about climate change impact on deltaic areas (see Sect. 2.6).

2.1 Case Study Area

The proposed methodology is applied in the deltaic area of the transboundary Mesta/Nestos river basin. The basin is almost equally shared both in terms of river's length (234 km in total) and basin's extent (5613 km^2) between Bulgaria and Greece, which are the upstream and downstream countries, respectively [54]. The river's water is used for hydropower production, irrigated agriculture and maintenance of the environmental flow. The delta covers about 55,000 ha, while the coastline is about 50 km long (Fig. 2). The regional economy is based on the primary sector (agriculture and fishery), while the tertiary sector (tourism and services) is developed but rather limited. Regarding the irrigated agriculture of the delta, the river's water is distributed through eight collective irrigation networks for the irrigation of 20,000 ha. Maize (37.1%), forage plants (13.5%), energy crops (13.5%), tree crops (10.1%), rice (8.8%), asparagus (4.8%), and wheat together with other types of cereals (4.0%) are the main cultivations. The river's delta is a very important EU wetland, with a large portion of the delta to be under the Ramsar Convention (10,593 ha), as well as more than 25% of the area to be nominated as an important region of the Natura 2000 network.

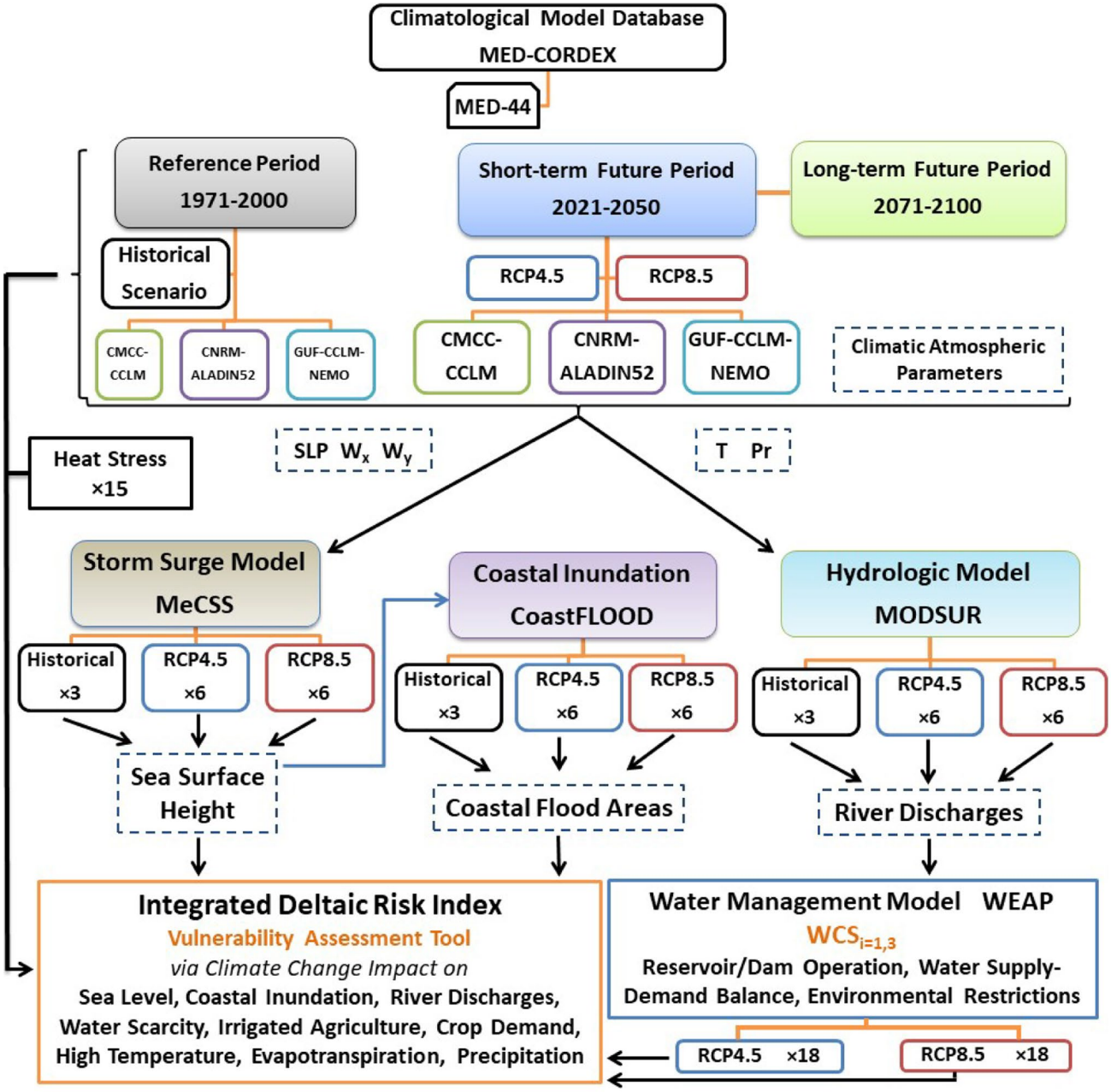

Fig. 1 Schematic representation of data flow within the proposed modeling approach for the estimation of an Integrated Deltaic Risk Index as a vulnerability assessment tool concerning the climate change impact on water resources management of the Nestos river delta site. SLP, atmospheric pressure at sea level; W_x, W_y, horizontal wind velocity components; T, atmospheric temperature; Pr, precipitation; WCS, water consumption scenario; Number of implementations for every model realization are given, e.g., as × 3, × 15, for each scenario/period

2.2 Climate Change Models and Scenarios

The climatic parameters, used as forcing to the maritime hydrodynamic and hydrological models, consist of wind (velocity and direction) and sea level pressure (SLP) fields, together with temperature and precipitation, respectively. They are derived by three high-resolution Regional Climate Models (RCMs) with a spatial resolution of 0.44° in a rotated pole projected geographic system. The RCMs have been developed and implemented in the framework of the MEDiterranean COordinated Regional climate Downscaling EXperiment (MED-CORDEX) initiative [55] (Table 1). For the evaluation of climate change impact on the case study area, atmospheric parameters from RCMs

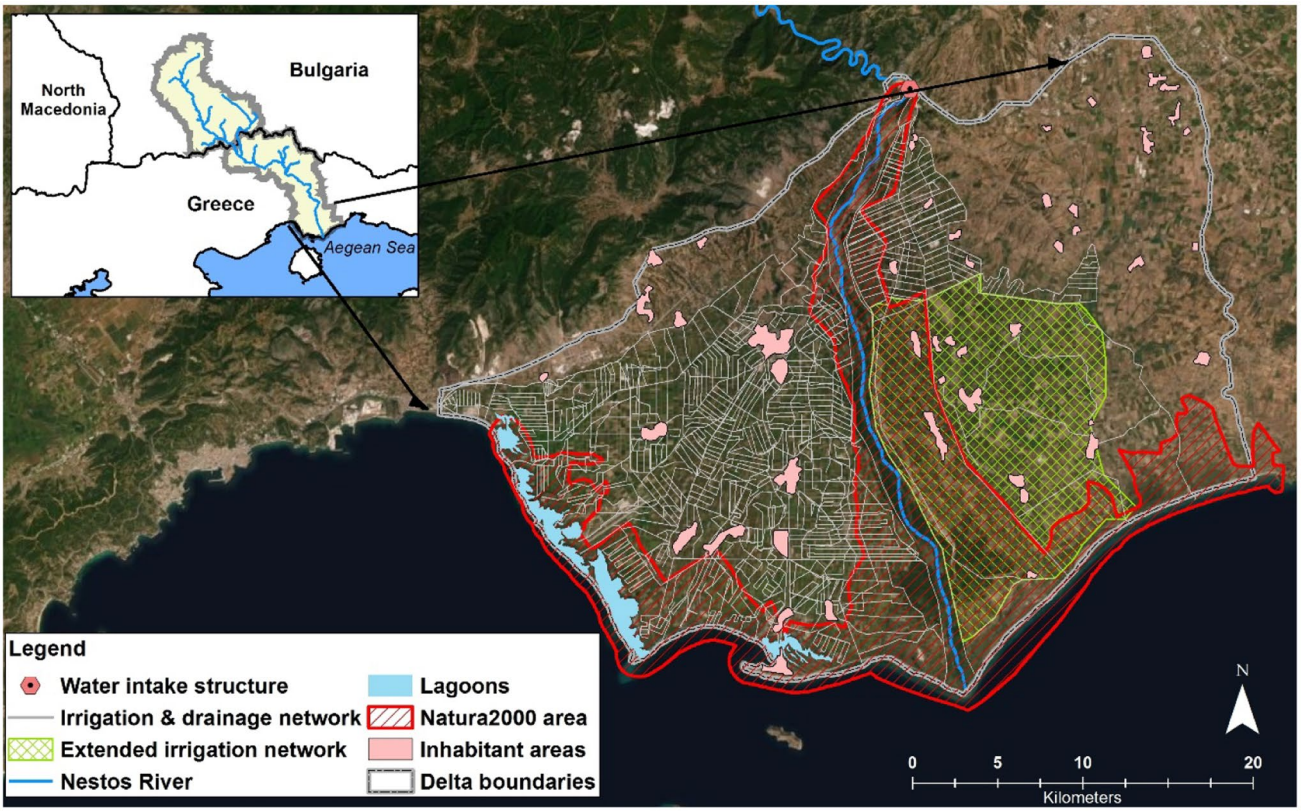

Fig. 2 Illustration of the Nestos river deltaic area including the existing irrigation network (grey lines), the future water reclamation project (green crosshatch polygon), the inhabitant areas (pink patches), the Natura 2000 protected areas (red hatched extent) and the coastal lagoons (cyan patches)

driven by two representative concentration pathways (RCPs) by the IPCC-AR5 for the twenty-first century, namely RCP4.5 and RCP8.5, were used for the future periods 2021–2050 and 2071–2100. RCP4.5 describes a possible future climate that depends on "modest" estimations about greenhouse gas concentrations in coming years, while RCP8.5 poses a "worst case scenario" [55]. The RCM hindcasts for the period 1971–2000 were also used for interpreting the future climatic variability.

Table 1 Regional climate model synoptic description

Regional climate model	Abbreviation in the paper	Regional climate model short description
CMCC-CCLM4-8-19 v.1	CMCC	CCLM is the COSMO-Climate Limited-area Modeling RCM tool, where COSMO is the sub-abbreviation for COnsortium for Small scale Modeling CCLM. That non-hydrostatic model delivers almost 100 consistent climate parameters [58]. It has been thoroughly validated and inter-compared with other RCMs [59].
CNRM-ALADIN52 v.1	CNRM	ALADIN is the limited area version of the ARPEGE model; hence, it is a limited area bi-spectral numerical climate model [60]. The model also uses ERA40 re-analysis to study regional climate processes, air-sea flux over the Mediterranean at regional scales, test of physical parameterizations, and produce regional climate change scenarios.
GUF-CCLM-NEMO4-8-18 v.1	GUF	CCLM-NEMO is an atmospheric-ocean circulation ensemble model collaboration of CCLM with NEMO (Nucleus for European Modeling of the Ocean), which is a pan-European community ocean-modeling framework. It is in use in a wide variety of applications whose prime objectives are oceanographic and climate research, operational ocean forecasts and seasonal weather forecasts [61].

In order to correct the biases of precipitation, one of the parameters with the highest degree of biases [56], a linear correction method was implemented. In particular, when using the linear correction method, RCM daily precipitation amounts, P, are transformed into P_* such that $P_*=aP$, using a scaling factor, $a=O/P$, where O and P are the monthly mean observed and RCM precipitation of the same grid point, respectively. Hence, the method was implemented on the hindcast datasets and the derived monthly scaling factors were applied to the RCMs daily observation of that month, generating the unbiased daily time series. The linear correction method belongs to the same family as the "factor of change" or "delta change" method [57]. The hindcast temperature datasets were not bias corrected because of the high degree of correlation with the observed temperatures.

2.3 Modeling of Storm-Induced Sea Level and River Hydrology

2.3.1 Modeling of Sea Level Elevation and Coastal Inundation

The numerical models for the simulation of maritime and coastal hydrodynamics comprise two nested computational fields:

- Field A: the regional scale of the entire Mediterranean basin in terms of storm-induced sea surface height (*SSH*) and barotropic currents with a special focus on the coastal zone of the northern Aegean Sea. The required simulations were conducted with the use of the Mediterranean Climatic Storm Surge (MeCSS) model.
- Field B: the local scale of the coastal zone in the study area (Nestos river delta), pertaining the estuary and adjacent lagoons. The process was simulated with the CoastFLOOD module.

Regarding the coupling of the two models, the CoastFLOOD module is fed with MeCSS model output of sea level data as boundary conditions on the study area's coastline, lagoons' shoreline, and urban waterfront. Hence, it provides estimative results for possible extended inundation of low-land areas in the coastal zone, the rural plain, and the downstream river estuary due to extreme events of storm surge-induced flooding for each of the 30-year study period.

Field A refers to the implementation of the MeCSS model [33–35], i.e., the "climatic" version of the HiReSS (High Resolution Storm Surge) model, which is a 2-D horizontal, barotropic, hydrodynamic circulation model for high-resolution simulations of storm surges and related flows in large-scale, enclosed, or semi-enclosed water bodies [62, 63]. MeCSS simulates the meteorologically induced sea surface variations and depth-averaged currents by taking into account the following processes: (a) the inverse barometer effect, i.e., the response of sea level to atmospheric pressure gradient of large barometric systems; (b) the shear stresses of wind applied on the air–water interface; (c) the geostrophic effects of the Coriolis force; (d) the bottom friction on the ocean bed; (e) the internal shear forces due to horizontal eddies based on the eddy viscosity concept and the Smagorinsky model approach [64]. Herein, results are based on climatic model runs of the model for long term periods (e.g., 30-year periods between 1971 and 2100), and its spatial resolution is set at 1/20°. The atmospheric forcing, namely the winds at 10 m elevation from Mean Seal Level (MSL) and the SLP fields, are provided by the RCMs of the MED-CORDEX database. Both HiReSS and MeCSS model versions have been thoroughly validated in the recent past under different configurations of storm surge simulations by comparisons against field data of sea level by in situ tide-gauge measurements for long-term *SSH* maxima [33–35], sea level extremes [36], and storm-induced episodic *SSH* due to severe weather conditions [65].

Field B refers to the implementation of an extremely high-resolution, 2-D coastal inundation module (CoastFLOOD), coupled to MeCSS model, which resembles the established LISFLOOD-FP model for coastal plain flooding [66–68]. CoastFLOOD is a simplistic 2-D finite difference hydrodynamic module for coastal inundation induced by storm surges. The concept of the LISFLOOD-FP model has been thoroughly evaluated in the past and vastly applied in flood plains [69, 70]. The approach was combined with a classic wet/dry cell assignment technique for flood fronts over steep slopes [71, 72]. Hereby, only steady-state inundation situations were taken into consideration referring to constant sea level states of storm surge maxima events (with $SSH_{max} > 0.32$ m). These would occur once in each of the 30-year periods of study and would last for at least 21 h and up to 3 days. The module makes use of very fine spatial resolution ($dx = 5$ m) computational domain, namely derived by post-processing geospatial data from the digital surface model (DSM) and digital elevation model (DEM) of the Hellenic Cadastre.[3] Indicatively, the computational domain (Field B) consists of nearly $28{\cdot}10^6$ cells.

The 1-D flow equations for expanded inundation are solved for each front of a typical 2-D grid cell in order to provide a 2-D solution in each horizontal direction (on the zonal and meridional, x- and y-direction, respectively) of the flow [68]. Based on Bates et al. [66], the continuity equation corresponds to the mass conservation principle for the calculation of local water depth (free-surface height) in each gridded cell. The module is led to flow route estimation by a simplistic quad-tree search algorithm for upstream cells and a dry/wet cell storage code, based on the difference of

[3] https://www.ktimatologio.gr/en

hydraulic head between neighboring cells. The flow rate is derived by a Manning's law approach using the water surface elevation above land level incorporating bottom friction. The continuity and momentum equations for the calculation of the change in volume of flow are given in discretized form as follows [68]:

$$h_{i,j}^{t'} = h_{i,j}^{t} + dt \cdot \frac{Q_{xi-1,j}^{t} - Q_{xi,j}^{t} + Q_{yi,j-1}^{t}\}Q_{yi,j}^{t}}{dx \cdot dy}, \quad (1)$$

$$Q_{x(i,j)}^{t} = \frac{h_{flow}^{5/3}}{n} \cdot \left(\frac{h_{i-1,j}^{t} - h_{i,j}^{t}}{dx} \right)^{1/2} dy, \quad (2)$$

$$Q_{y(i,j)}^{t} = \frac{h_{flow}^{5/3}}{n} \cdot \left(\frac{h_{i,j-1}^{t} - h_{i,j}^{t}}{dy} \right)^{1/2} dx, \quad (3)$$

where Q^t is the volumetric flow rate on time step t between adjacent cells, e.g., (i,j) and $(i-1,j)$ in x-direction, explicitly derived at the cell fronts using a forward-time centered-space (FTCS) finite difference scheme decoupled in x- and y-directions (Q_x, Q_y); $h_{i,j}$ is the free-surface height of water at the center of cell (i,j); h_{flow} is the effective water flow depth between two neighboring cells, defined by the difference between the highest possible water level in the two cells and the largest bed elevation in these particular cells (e.g., $SSH_{\max} - z_{i,j}$); z is the cell bed elevation; n is the Manning friction coefficient (ranging between e.g., 0.018 or 0.022 for clean or gravelly earth pathways, to 0.035 for stony cobble lands and pasture, farmland floodplains, and up to 0.075 for heavy brush floodplains); t' is the next time frame of simulation $t' = t + dt$ (dt is the maximum stable time step calculated after Hunter et al. [67]); and dx and dy are the cell widths in zonal and meridional directions, typically having values of a few meters for shallow coastal areas [66].

2.3.2 Modeling of River Hydrology

The freshwater volumes that are discharged in the delta's neck were simulated with the use of the spatially distributed hydrological model MODelisation du SURface (MODSUR) [73]. The model consists of a densely spaced grid and the budget is computed in each grid cell using a system of four reservoirs responsible for the repartition of rainfall into runoff, infiltration evapotraspiration and soil water storage. The MODSUR's description is explicitly given in Skoulikaris et al. [74] and the hydrological model setup used herein, i.e., the model's calibration and validation based on observations from 1987 to 1995 is included in Lazoglou et al. [75]. Thereafter, the calibrated model was forced by the bias corrected climate change datasets of rainfall and temperature that originated from the CMCC, CNRM and GUF models and based on the respective RCPs. The input data were spatially allocated in the hydrological model's grid, in order to simulate the river's discharges for the future periods of 2021–2050 and 2071–2100. The RCMs' output for the past period 1971–2000 also triggered the hydrological model's reference implementations, with its outputs used as baseline levels for the evaluation of the future modelled river discharge trends.

Since 1996, the river's main course is hedged by two large hydropower plants (HPPs); thus, the future discharges were simulated both for the subbasins that are drained in the dams' reservoirs and the subbasins that are located downstream of the dams. Particularly, the simulated water discharges of the upstream of the dams' watersheds fed a dam operation simulation model, with the output of the latter to be accumulated with the simulated water discharges coming from the downstream of the dams' subbasins in order to assess the runoff reaching the delta (Fig. 3). The simulation of the two *en cascade* hydropower dams was realized with the Water Evaluation And Planning (WEAP) model [76]. Having specified the technical characteristics of the dams [77] and the inflows to their reservoirs from the MODSUR model, WEAP uses a linear programming solver to maximize satisfaction of demands, subject to demand priorities, mass balances, and other constraints [78]. The demand priorities of environmental flow, irrigation, and hydropower production, i.e., the water uses in the case study area, were set to 1, 2, and 3, respectively, as the priority operational rules of the dams. Since the construction of the two HPPs, no river flooding has been observed in the downstream part of the river.

2.4 Water Balance Simulation and Scenarios

The water supply and demand balance operation in the deltaic area were also simulated with the WEAP model. The latter operates on the basic principle of water balance on a monthly and annual basis and illustrates an integrated aspect of a water system, both in its current state and in estimated future scenarios [76, 79]. The simulations were performed at a monthly time step to investigate the intense seasonal fluctuation of both water supply and demand within the deltaic area. The study timeframe includes the 1971–2000 reference period (RP), the 2021–2050 short-term future (STF), and the 2071–2100 long-term future (LTF) periods of climate projections.

Three different water consumption scenarios (WCS) are investigated regarding the management of the available water quantity and the estimation of the irrigation demands:

- WCS-REF reflects the river's discharges (water availability) under climate change, but it is assumed that the annual irrigation water demand remains stable and similar

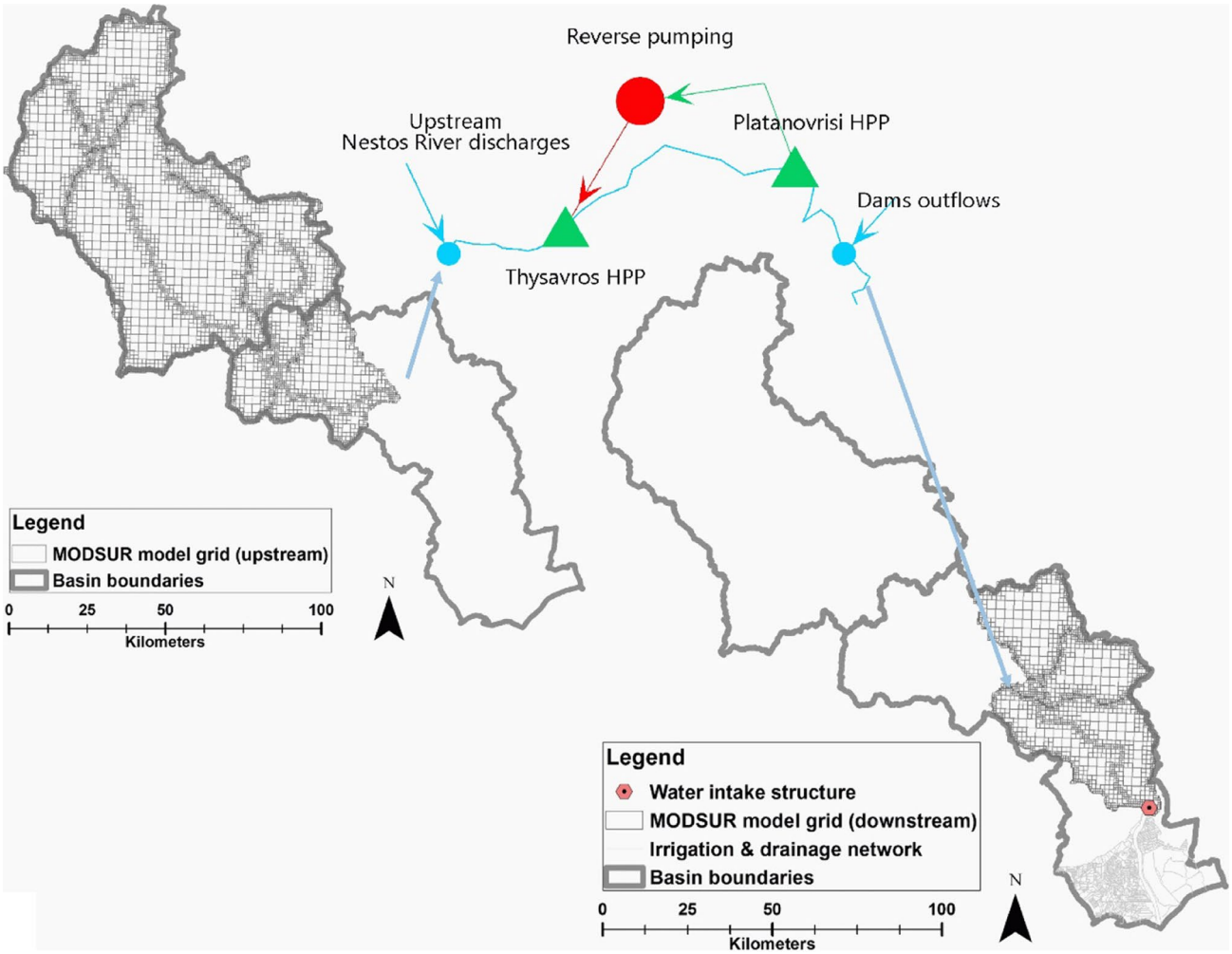

Fig. 3 Illustration of the Nestos River runoff simulation process: (i) application of the hydrological model to the watersheds draining into the HPPs' reservoirs (upper-left part of the figure), (ii) hydropower simulation with the use of operational priority rules (coloured part of the illustration), and (iii) accumulation of the dams' outlets with the simulated runoff derived from the downstream of the dams' watersheds to estimate the water reaching the water intake structure that is located in the beginning of the delta area (right part of the illustration)

to the current one. The demand is defined by the local Land Reclamation and Improvement organizations[4] and is equal to 1935 m^3/year/ha, including losses [77].

• WCS-CC proposes the assessment of irrigation demands under climate change as well as the implementation of sustainable irrigation practices. The calculation of the future crop's net water needs, depending on the cropping pattern and the climate, is based on the following equations:

$$I_n = \mathrm{ET}_c - (P_e + G_w + \mathrm{SM}), \tag{4}$$

$$\mathrm{ET}_c = K_c \times ET_o, \tag{5}$$

$$\mathrm{ET}_o = 0.0023 \times R_a \times (T + 17.8) \times (T_{max} - T_{min})^{0.5}, \tag{6}$$

$$P_e = f(D) \times \left(1.25 \times P_t^{0.824} - 2.93\right) \times 10^{0.000955 \cdot \mathrm{ET}_c}, \tag{7}$$

where I_n is the net irrigation water requirement; ET_c is the crop evapotranspiration under standard conditions [23]; G_w is the contribution of capillary elevation of groundwater; SM is the stored water amount in the crop root zone at the beginning of the growing season; K_c is the coefficient determining crop characteristics; ET_o is the reference crop evapotranspiration [80]; T, T_{max}, and T_{min} are the mean, maximum and minimum daily air temperature (h=2 m); and R_a is the daily total extraterrestrial solar radiation. The specific method offers a satisfying degree of result reliability and has been applied in various cases [81–83]. P_e is the effective rainfall based on monthly crop evapotranspiration

[4] https://lri.swri.gr/index.php/en/

and mean monthly rainfall, while P_t is the total precipitation, and $f(D)$ is a factor dependent on the maximum root moisture deficit (D is the yielded value of soil moisture content decline, up to the consequent irrigation water dosage). The third term of Eq. 7 ranges between 1 and nearly 1.1 (depending on, e.g., $ET_c \approx 0$–45 mm/day).

- WCS-EXT is primarily based on the WCS-CC and furtherly proposes the investigation of development policies in the delta's agricultural sector through the extension of the current irrigated area by 50%, in an attempt to exploit the excess water volumes that are identified when sustainable agricultural patterns are adopted. The specific measure is proposed as a development measure within the corresponding River Basin Management Plan [84] of the WFD implementation process.

2.5 High Temperature Stress Assessment

Daily temperature data from all RCMs, RCPs, and time periods (RP, STF, LTF) have been analyzed and assessed to identify HT occurrence and investigate the effects of thermal stress on specific crop species of the study area, namely maize, wheat, forage plants (soybean), and rice, which occupy 64.2% of the total cultivated area. Concerning maize, the investigation is related to cases that the predicted maximum daily temperature: (a) ranges from 33 to 40 °C for 15 days during the pre-anthesis and silking onwards growth stage [85], and (b) exceeds 35 °C for 14 consecutive days during the reproductive stage [86]. Wheat crop faces major effects of heat stress (e.g., shortened duration of grain filling and maturity, reduced leaf size) if temperature exceeds 38 °C (for 24–48 h) during the seedling stage and 37 °C for 20 days throughout grain filling and maturity stage [87]. Soybean is heat stressed if temperature exceeds 38 °C for 14 days during the flowering stage [88]. For rice cultivation, decreased yield is expected if temperature reaches 42.5 °C during the vegetative growth stage [89]. Particularly, with regard to maize cultivation in the study area, it has already been observed that temperature increase above 35 °C for a prolonged period ($e.g. \geq 2$ weeks) during the reproductive stage has a severe negative effect on the crop yield and causes significant production decline, according to estimates by the Directorate for Regional Agricultural Economics and Veterinary, under the authority of the Region of Eastern Macedonia and Thrace.[5] The results of the analysis concern the agricultural area that is affected by thermal stress per year and the probability of HT occurrence per crop and study period, for every possible combination among all RCMs, RCPs, and WCSs.

[5] https://www.pamth.gov.gr/index.php/en/

2.6 Integrated Deltaic Risk Index

Within the proposed conceptual framework, an approach of relating the investigated hazards with each corresponding study area's exposure probability is adopted [41, 42, 90]. To this end, the assessment of a risk index for each of the investigated hazards took place, which is determined by the product of the modelled hazard's magnitude (e_i) and the corresponding estimated probability of occurrence (p_i) in vulnerable parts of the Nestos river deltaic area (Fig. 2). Hence, the calculation of an Integrated Deltaic Risk Index (IDRI) was opted for, defined by the geometric mean of individual risk variables as follows:

$$IDRI = \left(\prod_{i=1}^{n} e_i p_i\right)^{\frac{1}{n}} \tag{8}$$

Altogether, three separate risk indexes based on the three identified types of hazards are incorporated in the present analysis as:

1. The Coastal Flood Risk Index (CFRI) refers to large-scale coastal inundation by extreme storm surge events. CFRI is defined by the seawater flooded area and the corresponding flood probability, derived with the coupled MeCSS-CoastFLOOD model.
2. The Water Scarcity Risk Index (WSRI) refers to the deficit in irrigation demand coverage in agricultural lands of the delta. WSRI is defined by the agricultural area that is not irrigated and the related water deficit probability. The relevant outputs were produced by the coupled hydrological and water balance models (MODSUR and WEAP).
3. Heat Stress Risk Index (HSRI) refers to the thermal stress effect on farming land, expressed by the heat stressed agricultural area and the related HT occurrence probability. HT magnitudes and heat stress assessment were derived from the statistical post-processing (by Peak-Over-Threshold method) of the MED-CORDEX atmospheric climate data.

All identified risk indexes are classified by the equidistant interval method, thus dividing the hazard magnitude datasets into a specified number of groups, distributing the amount of information between minima and maxima magnitudes of extreme events, in each 30-year period, over those groups evenly. Hence, the index values follow a classification ranging from very low to very high risk (corresponding to 1–5 ranks). Furthermore, the $IDRI = \sqrt[3]{(CFRI \cdot WSRI \cdot HSRI)}$ and its three aforementioned sub-risk component indexes were calculated for each combination of RCM, RCP, WCS, and time period leading to 39 implementation cases in total (3 for historical data and 36 for the future scenarios).

3 Model Validation

3.1 MeCSS Model Verification

Available in situ measurements of sea level variations from tide-gauge stations in the vicinity of the study area (northern Aegean Sea) by the Hellenic Navy Hydrographic Service[6] were used to evaluate the MeCSS model's performance. Statistical indexes and measures of inter-annual extreme values and intra-annual maxima of *SSH*, from both historical field data and storm surge modeling output, are compared herein. The recording periods correspond to an 11-year period, namely from 1995 to 2005. Daily averaged *SSH* values, used in the study, were derived from the measured data after subtraction of the MSL, which was determined using a moving average technique and a high-pass filter operator with a cut-off frequency of 1/30 days. This was done in order to exclude noise in the *SSH* signal from slow processes of long-term MSL oscillations due to steric effects in the Mediterranean basin [32, 91]. Field data series are also detided (removed astronomical tide signals) with the use of the *T-Tide* software [92] as MeCSS was run in non-tidal mode for the 1971–2100 study period.

3.1.1 Intra-annual Maxima

Comparisons of model against field data are based on intra-annual storm surge maxima, e.g., Storm Surge Index (*SSI*), which is defined as the average of the three highest independent events (separated by at least 120 h) of storm surge maxima per year [32] for all modelled and observed 11-year time series. Percentage error factors and error indexes (*E*, *EI*, and RMSE) of *SSI* time series were also calculated as follows:

$$E(\%) = 100 \cdot \left(\overline{SSI_{\text{mod}}} - \overline{SSI_{\text{obs}}}\right) \Bigg/ \left(\frac{\overline{SSI_{\text{mod}}} + \overline{SSI_{\text{obs}}}}{2}\right), \tag{9}$$

$$\text{EI} = \left(\overline{SSI_{\text{mod}}} - \overline{SSI_{\text{obs}}}\right) \Bigg/ \sqrt{\left(\sigma^2_{SSI_{\text{mod}}} + \sigma^2_{SSI_{\text{obs}}}\right)/2}, \tag{10}$$

$$\text{RMSE} = \sqrt{\sum_{i=1}^{N} \left(SSI_{\text{mod},i} - SSI_{\text{obs},i}\right)^2 \Big/ N}, \tag{11}$$

where over-barred SSI_{mod} and SSI_{obs} are the time-averaged *SSI* as derived from modelled and observed data, respectively; σ is the mean standard deviation of *SSI*; and *E* is obviously positive when MeCSS overestimates the amplitude of the sea level elevation against observed data. Comparisons refer to the closest station to the Nestos river delta with available in situ monitoring by a tide-gauge device, namely Alexandroupoli port in the northeastern Aegean Sea coastal region. MeCSS model forced by MED-44 resolution MED-CORDEX climatic data for the RP slightly underestimates the magnitudes of intra-annual *SSH* maxima and *SSI*. The percent errors (> 15%) are quite high in the study region, but acceptable for climatic mode hindcasts during the 11-year part of the reference period (Table 2).

Table 2 Evaluation of MeCSS model implementations by different climatic forcing input based on error percentage and index (E and EI) of parameters: (a) SSH_{max} and (b) *SSI* in the Alexandroupoli station

Parameters	*a*		*b*	
Input	Mean E_i (%)	Mean EI_i	Mean E_i (%)	Mean EI_i
CMCC-MeCSS	− 18.71	− 0.651	− 16.92	− 0.519
CNRM-MeCSS	− 27.47	− 1.020	− 21.57	− 0.699
GUF-MeCSS	− 23.03	− 0.860	− 17.20	− 0.561

The absolute yearly maxima of sea level variations were investigated using the 11-year average of annual SSH_{max} of both simulated and observed time series. Same comparisons as for the *SSI* were performed providing similar results. Overall, the cumulative comparison of measured and simulated 11-year mean SSH_{max} for the three MeCSS implementations reveals that CMCC-forced MeCSS runs

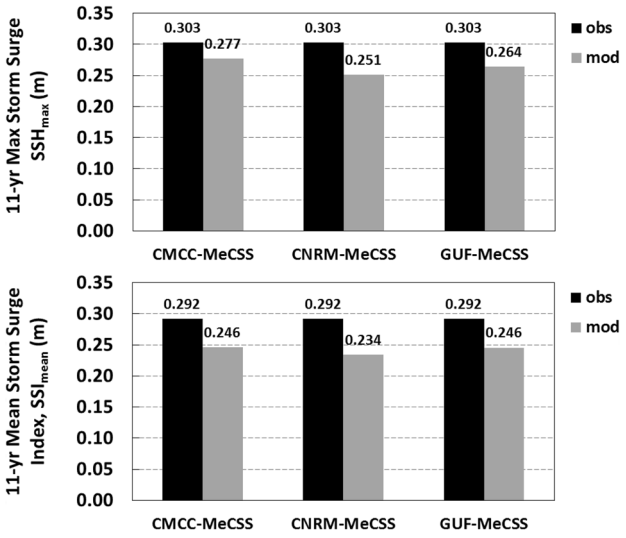

Fig. 4 Evaluation of MeCSS model implementations by different climatic forcing input based on comparisons of 11-year maximum *SSH* (m) (upper graph) and average *SSI* (m) (lower graph) in the Alexandroupoli station for modelled (mod) and field (obs) storm surge data

[6] http://www.hnhs.gr/portal/page/portal/HNHS

perform slightly better than the rest climatic implementations (Fig. 4).

3.1.2 Probabilities of Occurrence of Storm Surges

For the assessment of the probabilistic properties of the modelled *SSH* time series, a heuristic approach is used in the present study; a statistically coherent event is defined as having threshold values of $SSH_{coh} \geq (\mu_{SSH} + \sigma_{SSH})$, where μ is the mean of the *SSH* time series over the entire study period, and σ is the corresponding standard deviation [35, 36]. The exceedance probability (P_{coh}) of the critical value for coherent events together with the respective thresholds are presented in Fig. 5, as derived from both simulated and observed time series. In addition, the exceedance probability of intense and extreme events (P_{int} and P_{ext}), which are defined as $SSH_{int} \geq (\mu_{SSH} + 2\sigma_{SSH})$ and $SSH_{ext} \geq (\mu_{SSH} + 3\sigma_{SSH})$, are also presented.

Simulated values are correlated well with the measured ones, indicating the acceptable performance of the MeCSS model. Specifically, the performance of all model setups is good with the GUF-forced MeCSS providing the best results for extreme values of *SSH*. Both CMCC- and CNRM-forced MeCSS perform better for coherent and intense events. Overall, it can be deduced that the MeCSS model can adequately reproduce the storm surge patterns for all the classes of statistical thresholds. Therefore, the reproduced probabilistic parametric features of the modelled *SSH* data can be considered to be reliable for further use in coastal vulnerability analysis presented in the following.

3.1.3 Inter-annual Maxima

For the quantitative assessment of the MeCSS model ability to reproduce *SSH* values and thus decide on the need of bias correction for modelled storm surge results, the calculation of the Hit-Rate-of-Percentiles index (*HRP*-index) [24] took place. Namely, the *HRP*-index computes the absolute differences between sorted (1st–99th) percentiles of simulated and observed values of *SSH*, and it is defined as the sum of all categorical fractions, i.e., differences compared with an allowed deviation. The latter was taken as the average

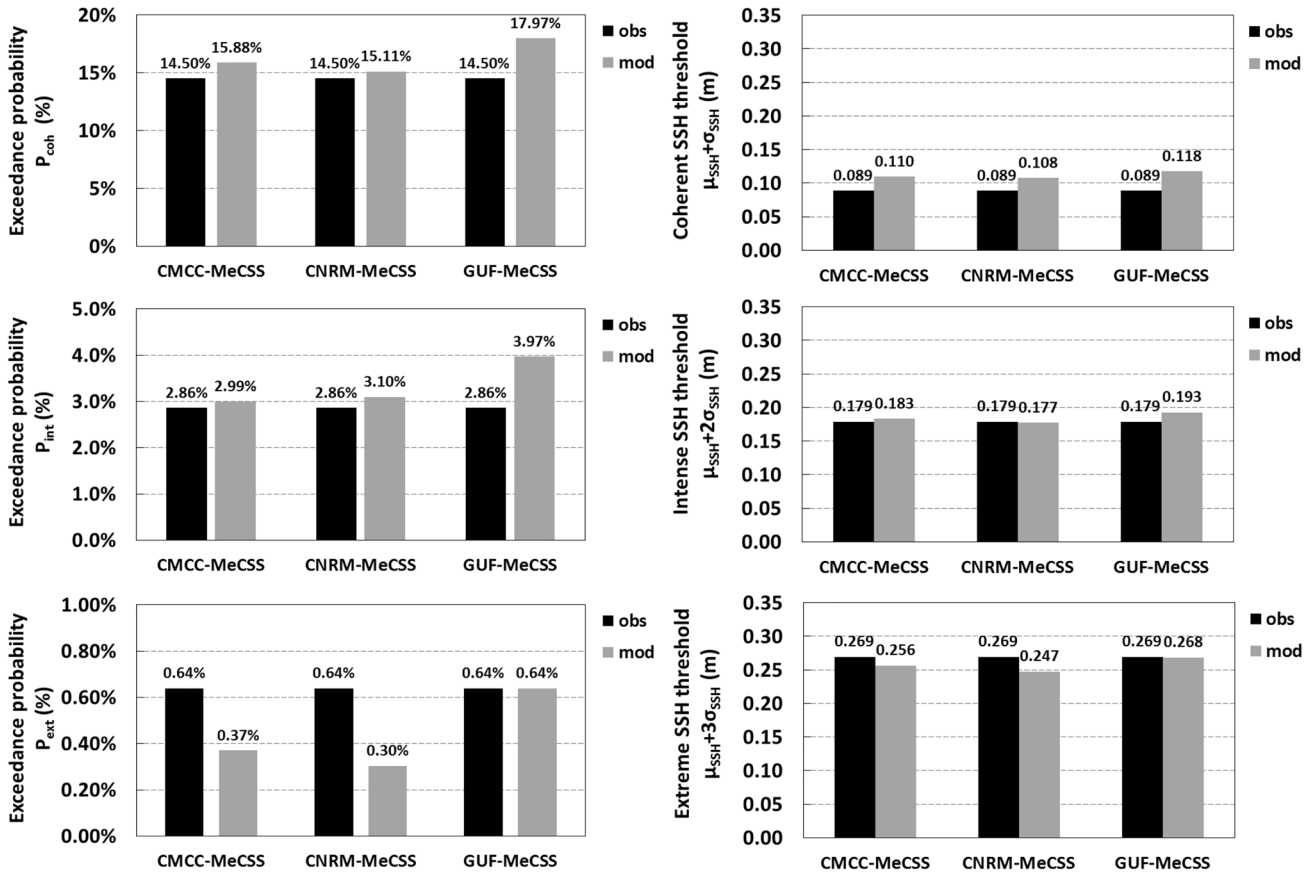

Fig. 5 Evaluation of MeCSS model implementations by different climatic forcing input based on comparisons of exceedance probabilities of coherent, intense, and extreme events of storm surges (left graphs) and respective *SSH* thresholds of μ_{SSH} and σ_{SSH} summations (m) (right graphs) in the Alexandroupoli station for modelled (mod) and field (obs) storm surge data

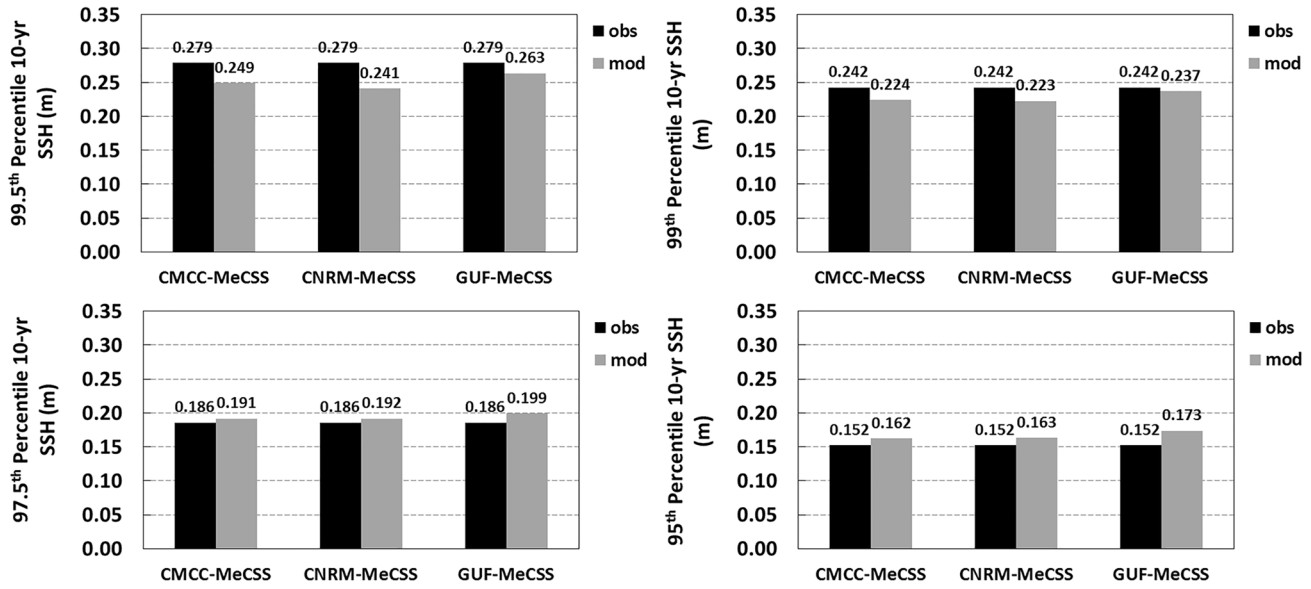

Fig. 6 Evaluation of MeCSS model implementations by different climatic forcing input based on comparisons of high-order percentiles of *SSH* (m) in the Alexandroupoli station for modelled (mod) and field (obs) storm surge data

of standard deviations of all modelled and observed *SSH* time series (σ_{SSH}). If *HRP*-index (ranging between 0 and 1) scores greater than 0.95, then the model efficiently is considered to efficiently represent the regarded observation time series (simulated datasets do not need bias corrections). The derived *HRP*-index for the Alexandroupoli station takes values from 0.95 for the CNRM-forced MeCSS model run to 0.98 and 1 for the GUF- and CMCC-MeCSS implementation, respectively. Therefore, it can be deduced that MeCSS model can adequately simulate the statistical properties of the ranked percentiles of *SSH* in a characteristic location of the interest area (northern Aegean Sea coastal zone).

To enhance the validation analysis and comparisons of storm surge maxima, the inter-annual extremes of the available time series were used. Thus, the performance of the MeCSS model was also evaluated using high-order percentiles (95th, 97.5th, 99th, 99.5th) of *SSH* for both modelled and observed time-series; comparisons are presented in Fig. 6. In general, all model implementations

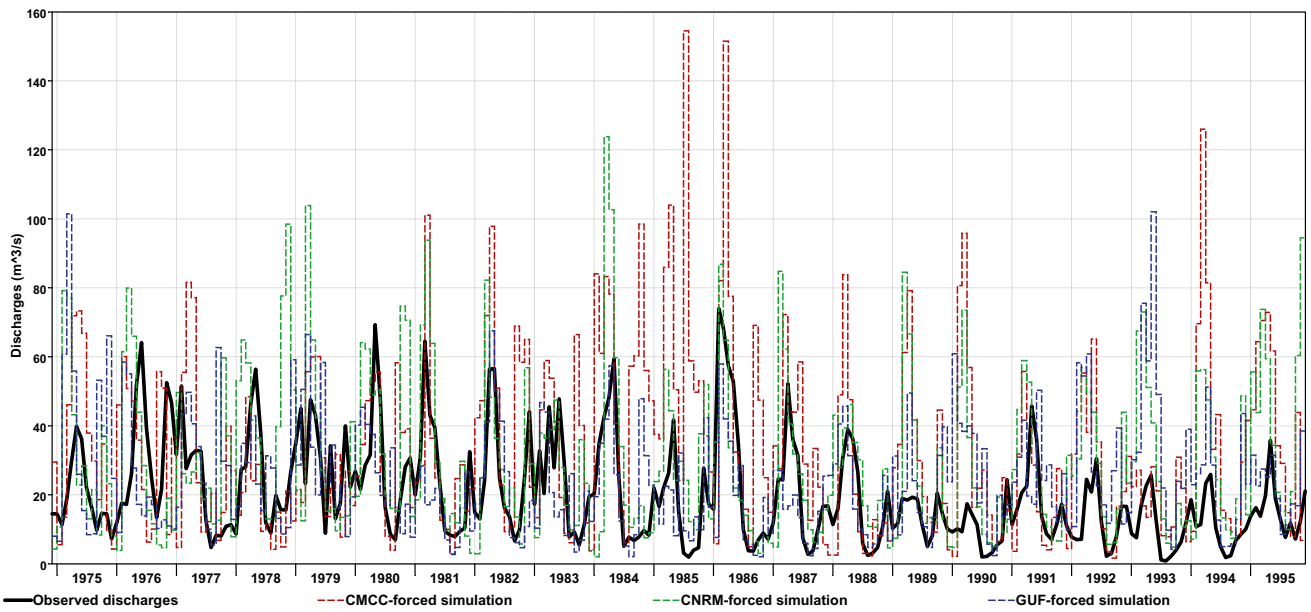

Fig. 7 Simulated MODSUR river discharges forced by the CMCC (red dotted curve), CNRM (green dotted curve), and GUF (blue dotted curve) climate models' hindcasts in comparison with the observed discharges (black solid curve) at the BG-GR borders for the period 1975–1995

Table 3 Statistical analysis of the simulated river discharges forced by the CMCC, CNRM, and GUF models and the observed discharges (OBS) at the political borders of the Nestos river basin, for the period 1975–1995

Statistical measures	CMCC to OBS	CNRM to OBS	GUF to OBS
Pearson correlation r	0.393	0.518	0.27
RMSE (mm)	28.527	22.686	20.135
Maximum discharges (mm)	154.49	123.81	102.0
RMSE/maximum	18.47%	18.32%	19.73%

perform well (especially for the 95th to 99th percentiles of *SSH*), with a tendency to overestimate the lower percentiles only marginally (by almost 2–8%) and slightly underestimate (by almost 6–15%) the higher ones closer to the *SSH* maxima. Therefore, it can be deduced that the agreement of the MeCSS model runs for all model implementations is high in terms of unfiltered *SSH* extremes reproduced in the 11-year simulation period of 1995–2005. The GUF-MeCSS model setup outperforms the other two in terms of maxima, but CMCC- and CNRM-MeCSS implementations behave more plausibly for lower values of storm surge levels.

4 Hydrosystem Model Verification

4.1 MODSUR Model Verification

The comparison of the observed and the simulated discharges was conducted for a station located at the Greek–Bulgarian borders for the period 1975–1995, where monthly flow measurements were available [75] (Fig. 7). For that period, the mean monthly observed discharge equals 20.39 m^2/s, while in the cases of CMCC, CNRM, and GUF data, the 21-year mean discharges were computed as 34.11 m^2/s, 30.45 m^2/s, and 24.87 m^2/s respectively, i.e., an overestimation of 40.2%, 33.1%, and 18.1% per climate model, respectively. The GUF-triggered simulated discharges, nevertheless, have a relatively high correlation with the observed discharges in terms of minimum values.

The statistical measures of Pearson correlation coefficient, i.e., the covariance of the observed and simulated datasets divided by the product of their standard deviations, and of RMSE (see Eq. 11; here corresponding to river discharges), are introduced within Table 3. The simulations with the use of the CNRM-forced output data present the best correlation with the observational datasets, while the smallest one is presented in the case of the GUF-driven MODSUR results. On the other hand, the GUF-driven outputs present the best correlation in terms of annual minimum flows (Pearson's $r = 0.54$), while for the maximum values the best fit is demonstrated with the CNRM-forcing (Pearson's $r = 0.44$). The quotient RMSE/MAX for all the selected RCM-driven cases is less than 20.0%, a figure that is considered relatively low and supports the utilization of the specific hydrologic output for further IDRI evaluations.

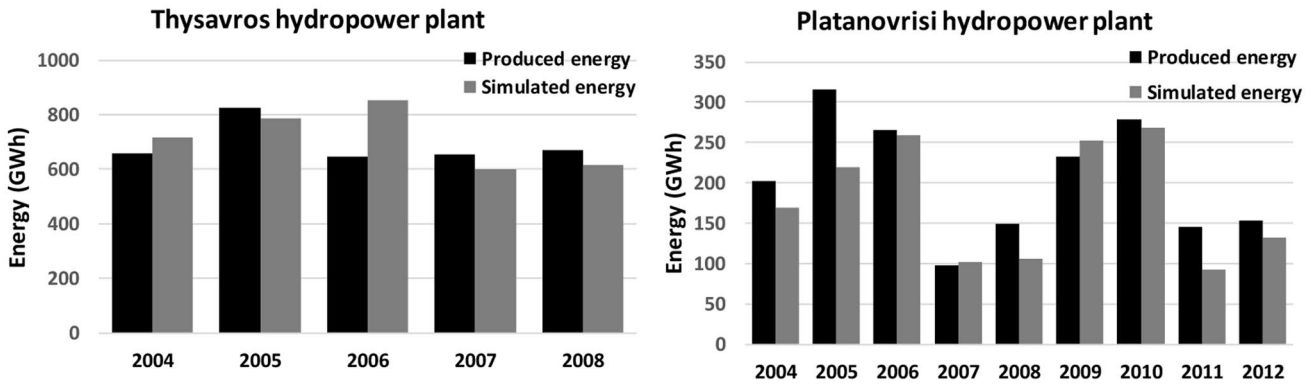

Fig. 8 Validation of the WEAP model for the upstream (left bar diagram) and the downstream (right bar diagram) hydropower plants of the Nestos River based on energy production data

Table 4 MeCSS model results of (A) SSH_{max} (m), (B) differences Diff (%) between climatic scenario runs and RP levels (LTF-RP, STF-RP for each RCP), and (C) Diff (%) by various MeCSS input as CMCC-, CNRM-, and GUF-forced storm surge implementations on the coastal zone of the Nestos river delta

Study case		A			B			C		
Scenario	Period	CMCC MeCSS SSH_{max} (m)	CNRM MeCSS SSH_{max} (m)	GUF MeCSS SSH_{max} (m)	CMCC MeCSS Diff (%)	CNRM MeCSS Diff (%)	GUF MeCSS Diff (%)	CMCC-CNRM MeCSS Diff (%)	CNRM-GUF MeCSS Diff (%)	GUF-CMCC MeCSS Diff (%)
Historical	RP	0.367	0.331	0.397	0	0	0	10.37	− 17.98	7.65
RCP4.5	STF	0.368	0.339	0.390	0.20	2.36	− 1.77	8.24	− 13.88	5.66
RCP4.5	LTF	0.326	0.334	0.371	− 11.39	0.71	− 6.55	− 2.42	− 10.54	12.95
RCP8.5	STF	0.346	0.361	0.341	− 5.78	8.99	− 14.10	− 4.18	5.77	− 1.60
RCP8.5	LTF	0.341	0.345	0.371	− 7.27	4.25	− 6.39	− 1.33	-7.27	8.59

4.2 WEAP Model Validation

The validation of the WEAP model, used for the simulation of the hydropower plants' operation, was conducted based on produced energy data, expressed in GWh, coming from the Independent Power Transmission Operator of Greece.[7] In particular, the upstream plant, namely Thysavros (Fig. 3), was validated against available data of the period 2004–2008, while the validation of the downstream plant, namely Platanovrisi (Fig. 3), which regulates the final outflows in the Nestos river main course, was based on data covering the period 2004–2012. The outputs, as depicted in Fig. 8, present high correlation between the real produced energy and the simulated one. For the upstream dam, the coefficient of determination (R^2) and the RMSE normalized with the highest annually produced energy were equal to 0.617 and 5.3%, respectively. For the Platanovrisi dam, i.e., the downstream one, R^2 and RMSE, normalized to the highest annually produced energy, were equal to 0.785 and 17%, respectively. The latter values are considered to range from good to acceptable rendering the simulated WEAP output as adequate for the following water supply analysis in the results section.

5 Results

5.1 Sea Level Elevation and Inundated Areas Under Climate Change

5.1.1 Episodic Storm Surge Maxima on the Shoreline

The storm surge levels used in our analysis of CCI, with the implementation of the IDRI, refer to 30-year *SSH* maxima on the shoreline derived from hydrodynamic modeling in the entire Mediterranean basin. Table 4 presents relevant MeCSS model results of SSH_{max} and calculated percentage differences between two future climatic scenario approaches (for both STF and LTF periods) and RP values; e.g., Diff (%) = (SSH_{max}^{STF}—SSH_{max}^{RP})/(SSH_{max}^{RP}), given in column B of Table 4. The differentiations due to various forcing input are also examined in couples between CMCC-, CNRM-, and GUF-forced storm surge implementations for each scenario/period case separately, e.g., Diff (%) = (SSH_{max}^{CMCC}—SSH_{max}^{CNRM})/Average$^{CMCC-CNRM}$, given in column C of Table 4. Results refer to the coastal zone of the Nestos river delta.

There is a rather consistent pattern that GUF-forced MeCSS overestimates SSH_{max} compared with the CMCC- and CNRM-MeCSS setups for almost all study periods. CMCC- and GUF-forced MeCSS produce results that confirm a tendency towards storminess attenuation (expected lower SSH_{max} from nearly − 2% down to − 14%) in the study region for the future under any RCP scenario. However, based on CNRM-forced MeCSS results, the storm surge maxima are estimated to increase (from inappreciable amounts up to 9%) for both scenarios in the two twenty-first century's study periods compared with the RP at the coastal zone of Nestos river delta. In general, for most of the combinations of RCP-scenario to MeCSS-implementation the predicted storm surge maxima of the LTF are estimated to be lower than those of the STF period, i.e., indicating a clear decrease of storm surge extreme levels towards the end of the twenty-first century compared with the first half of it. The derived 30-year SSH_{max} values of Table 4 are used as input in all the following analysis of coastal inundation modeling, flooded area maxima calculations, and deltaic vulnerability indexing.

[7] http://www.admie.gr/nc/en/home/

Table 5 MeCSS-driven CoastFLOOD (M-CF) model results of A) Flooded Area, FA (ha), B) respective differences Diff (%) between climatic scenario runs, and C) Diff (%) by different forcing input as CMCC-, CNRM-, and GUF-forced storm surge implementations. Explanation of Diff in description of Table 4

Study case		A			B			C		
Scenario	Period	CMCC M-CF FA (ha)	CNRM M-CF FA (ha)	GUF M-CF FA (ha)	CMCC M-CF Diff (%)	CNRM M-CF Diff (%)	GUF M-CF Diff (%)	CMCC-CNRM M-CF Diff (%)	CNRM-GUF M-CF Diff (%)	GUF-CMCC M-CF Diff (%)
Historical	RP	380.897	354.832	452.257	0	0	0	7.09	− 24.14	17.13
RCP4.5	STF	381.420	358.847	447.705	0.14	1.13	− 1.01	6.10	− 22.03	15.99
RCP4.5	LTF	352.045	356.615	382.425	− 7.57	0.50	− 15.44	− 1.29	− 6.98	8.27
RCP8.5	STF	365.465	377.780	359.442	− 4.05	6.47	− 20.52	− 3.31	4.97	− 1.66
RCP8.5	LTF	359.477	365.055	383.352	− 5.62	2.88	− 15.24	− 1.54	− 4.89	6.43

5.1.2 Coastal Inundation Areas and Maps

The sum of the potentially flooded low-land areas, corresponding to values of land elevation $z \leq 0.5$ m, in the study region of Nestos river delta was calculated to be 1803.758 ha. The potentially affected areas cover the entire coastal region adjacent and around the lagoons (see Fig. 2) and the airport of Kavala on the western part of the map. The easternmost low-land (touristic) coastal areas of Nestos delta also seem to be potentially susceptible to coastal inundation by storm surges but to a lower extent. All the possibly affected stretches are parts of the environmentally protected Natura 2000 areas of the study region (see Fig. 2).

The values of flooded areas (*FA*), pertained in the analysis of climate change impact and vulnerability indexing, refer to probably inundated areas due to 30-year maxima of *SSH* on the seafront. Initially, the maximum reference level of possibly inundated coastal areas was determined as $FA = 541.69$ ha, which is equal to a 30.03% of the aforementioned determined low-land areas. The latter value endowed by CoastFLOOD simulationσ driven by maximum storm surge level, corresponding to a very high return value of an extreme storm surge event with $SSH_{\max} = 0.5$ m, respective of a very low probability of occurrence, e.g., 58×10^{-4}% [35, 36].

Subsequently, Table 5 presents the MeCSS-driven CoastFLOOD model results for *FA* (ha), and their respective calculated percentage differences between two future climatic scenario approaches (for both STF and LTF periods) and RP values. The differentiations, due to various forcing input, is also examined in couples between CMCC-, CNRM-, and GUF-forced coastal inundation implementations. There is a similar pattern for flooded areas as in the analysis of storm surges. It is rather obvious that GUF-forced CoastFLOOD overestimates the flood extents compared with the CMCC- and CNRM-forced setups for almost all study periods. The CMCC- and GUF-forced CoastFLOOD results again show a tendency towards attenuation of coastal floods, i.e., with rather low values < -8% for the first one and down to higher negative scores of -20% for the latter (under any future RCP scenario).

However, based on the CNRM-forced CoastFLOOD results, the inundation patterns in the study area are expected to remain close to the RF levels with a slight increase up to 6.5% under RCP8.5 for the first half of the twenty-first century. In general, for most of the combinations of RCP-scenario to inundation model implementation the predicted *FA* maxima of the LTF period are estimated to be lower than those of the STF period, i.e., indicating a clear decrease of extreme flood levels towards the end of the twenty-first century compared with the first half of it.

Figure 9 presents the estimated inundation areas due to storm surge based only on CMCC-forced MeCSS-driven CoastFLOOD simulations (others not shown for the sake of brevity) in the region of interest at the Nestos river delta. All the combinations of scenarios and periods of study are used, and the inundated areas of Fig. 6 correspond to the driving force of coastal storm surge maxima ($SSH_{\max}$) values of Table 4. A stable pattern of potential flooding in the study region is obvious from the past to the twenty-first century. Climate change-driven variations are not easily distinguishable visually, yet the most pronounced reductive changes concern the GUF-forced CoastFLOOD approach as revealed by the abovementioned quantitative analysis.

5.2 Coastal Inundation Probabilities at Vulnerable Areas Under Climate Change

For the identification of CCI (and the respective CFRI and IDRI calculations in Sect. 4.6), the established hazard (i.e., coastal inundation) was considered to occur as a steady-state saturated flood condition, thus only for storm surges driving effectively lasting flood events, i.e., with duration > 21 h and a threshold of $SSH_{\max} \geq z_m$. The latter (z_m) is defined as the median earth elevation z only for low-land (potentially flooded) areas from a very fine resolution DEM dataset

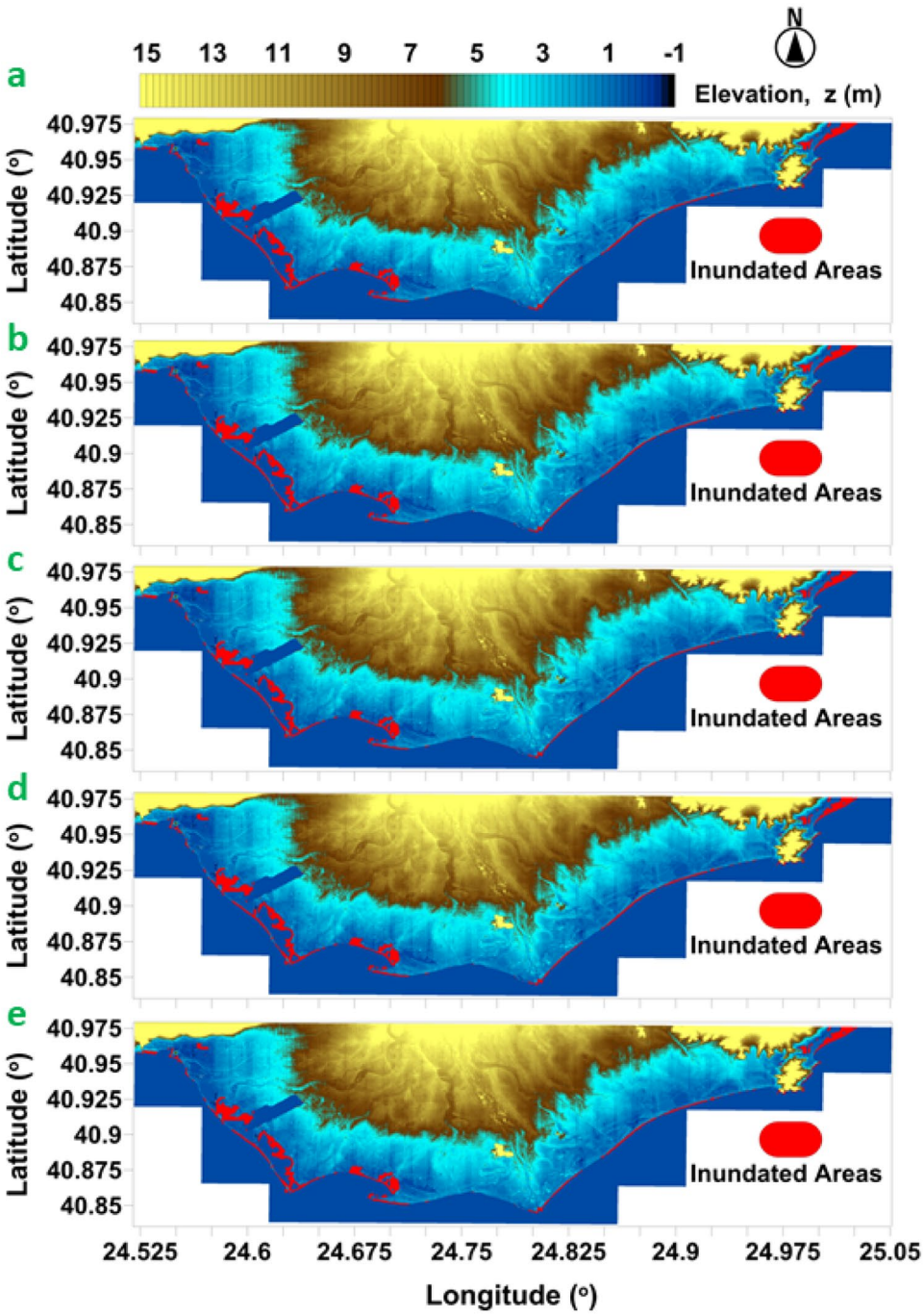

Fig. 9 Estimated inundation areas due to storm surge based on CMCC-forced MeCSS-driven CoastFLOOD simulations in the region of interest at the Nestos river delta; scenarios/periods: **a** historical (1971–2000), **b** RCP4.5 (2021–2050), **c** RCP4.5 (2071–2100), **d** RCP8.5 (2021–2050), **e** RCP8.5 (2071–2100)

(dx = 5 m) in the study region. Inundated areas were simulated, and respective flood probabilities were calculated for the modelled cases of storm surge levels exceeding this threshold.

Table 6 presents the calculated flood probability, FP (%), from MeCSS-driven CoastFLOOD results (marked as M-CF), and their respective calculated percentage differences between future climatic scenario implementations (for both STF and LTF periods) and RP values. The differentiations, due to three different RCM forcing datasets, are also examined in couples between CMCC-, CNRM-, and GUF-forced coastal inundation implementations. The pattern of flood probabilities remains akin to the previous findings for SSH_{max} and FA, yet with a more pronounced percentage of change. It is very clear that GUF-forced CoastFLOOD again overestimates by 80–200% the flood probability compared with the CMCC- and CNRM-forced setups for all study periods. The tendency towards

Table 6 MeCSS-driven CoastFLOOD (M-CF) model results of (A) flood probability FP (%), (B) respective differences Diff (%) between climatic scenario runs, and (C) Diff (%) by different forcing input as CMCC-, CNRM-, and GUF-forced storm surge implementations. Explanation of Diff in description of Table 4

Study case		A			B			C		
Scenario	Period	CMCC M-CF FP (%)	CNRM M-CF FP (%)	GUF M-CF FP (%)	CMCC M-CF Diff (%)	CNRM M-CF Diff (%)	GUF M-CF Diff (%)	CMCC-CNRM M-CF Diff (%)	CNRM-GUF M-CF Diff (%)	GUF-CMCC M-CF Diff (%)
Historical	RP	0.15	0.09	0.35	0	0	0	44.90	− 115.18	80.72
RCP4.5	STF	0.09	0.01	0.35	− 38.66	− 91.58	0.86	168.00	− 191.21	117.86
RCP4.5	LTF	0.08	0.03	0.25	− 42.34	− 65.32	− 27.67	89.66	− 154.29	98.79
RCP8.5	STF	0.10	0.10	0.23	− 33.99	8.43	− 32.01	− 3.96	− 79.88	83.19
RCP8.5	LTF	0.04	0.05	0.15	− 73.23	− 46.90	− 57.42	− 22.72	− 99.49	115.67

attenuation of coastal flood probability of occurrence throughout the entire twenty-first century is prevalent in all modelled cases for all climatic forcing and scenario/period combinations. The decrease of coastal storm flood frequency of occurrence reaches down to nearly − 92% (e.g., for the STF period under RCP4.5). In general, the RCP8.5 scenario approach (unlike the RCP4.5) leads to very decreased estimated coastal flooding probabilities towards the end of the twenty-first century compared with the first half of it.

5.3 River Discharges Under Climate Change

The hydrologic simulation process for the future climate demonstrated different outputs for the two RCPs. As expected, in the RCP4.5 case, the overall decrease of the river discharges was smaller than in the RCP8.5 case. In particular, for the RCP4.5 scenario, shown in Fig. 10, the average river discharges by CMCC forcing at the borders of the two countries for the 30-year period of 1971–2000 (RP) were 33.2 m^3/s, with the discharges in the STF and LTF periods to be 4.1% and 19.9% lower than in the RP, respectively. Similar behavior is observed when the hydrological model is triggered by the GUF model's data. The average discharges for the RP were 24.4 m^3/s, while the discharges in the STF and LTF periods presented a decrease of 6.9% and 13.8%, respectively. On the other hand, the outputs for the CNRM-driven MODSUR outputs present an opposite trend, i.e., the discharges of the STF and LTF were 7.47% and 3.78% larger than the 30.1 m^3/s of the RP period.

In the RCP8.5 case (Fig. 11), and the CMCC forcing data, the average river discharges for the STF and LTF periods were 35.1 m^3/s and 18.5 m^3/s, i.e., 5.7% greater and 44.3% lower than 33.2 m^3/s of the RP respectively. When the hydrological model is triggered by GUF's RCM output, the river discharges in the STF and LTF periods presented a decrease of 20.5% and 40.7%, respectively in comparison to the RP discharges. Finally, the 29.7 m^3/s and 26.2 m^3/s of the STF and LTF periods for the CNRM driven simulations demonstrated a small decrease of 1.4% and 12.9%, respectively, in relation to the discharges of the RP period.

A further analysis of the simulated river discharges at the delta's neck, i.e., by accumulating the discharges of the downstream of the dams' watersheds is presented in Table 7. It is demonstrated that for both RCPs corresponding to the STF period, the CMCC-forced and CNRM-forced simulated discharges are close to the ones of the reference period (RP). For the CMCC-forced simulations, the fluctuation is from − 1.80 to + 6.55%, while these figures are turning to + 3.25 to − 6.03% for the CNRM-forced simulations. On the other hand, the GUF-forced simulations for the same period demonstrate

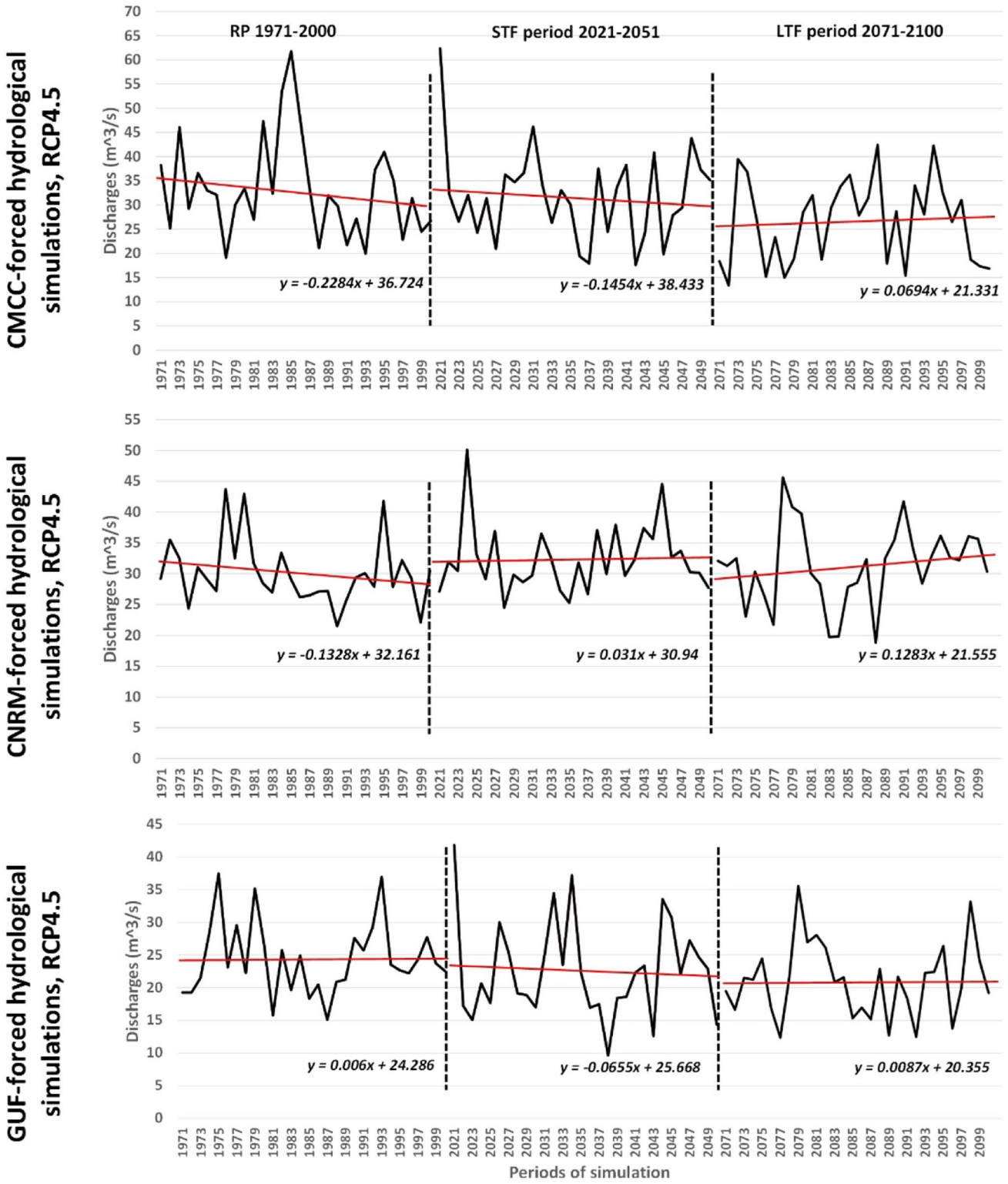

Fig. 10 Simulation results of annual river discharges at the Nestos River national borders based on hindcasts (RP time period) and RCP4.5 climate projections (STF and LTD time periods) for RCM-driven hydrologic implementations; CMCC-, CNRM-, and GUF-forced MODSUR model runs (upper, mid, and lower graphs, respectively). Linear trends are also presented (red color lines) together with their respective equations per simulation period

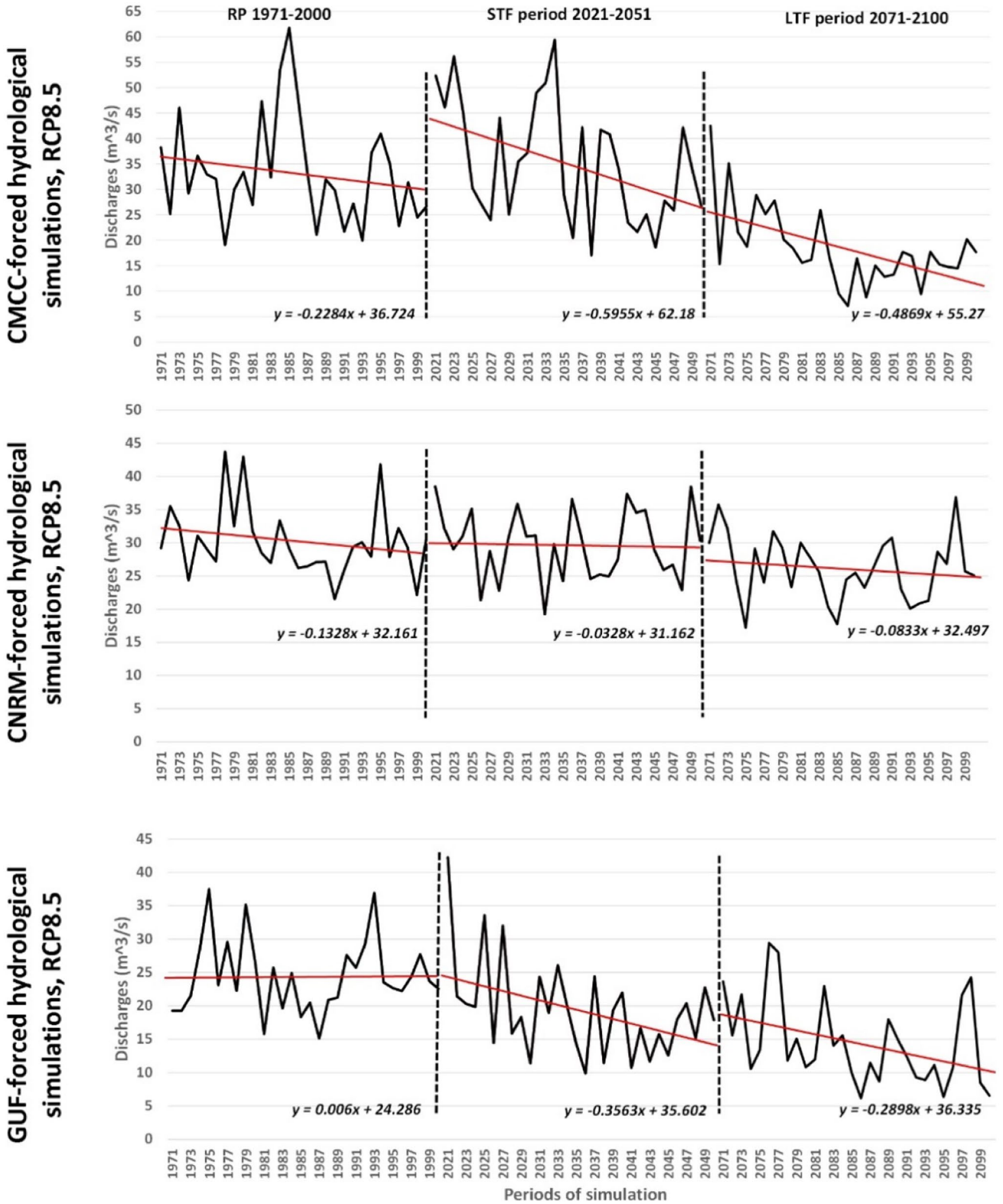

Fig. 11 Simulation results of annual river discharges at the Nestos River national borders based on hindcasts (RP time period) and RCP8.5 climate projections (STF and LTD time periods) for all RCM-driven hydrologic implementations; CMCC-, CNRM-, and GUF-forced MODSUR model runs (upper, mid, and lower graphs, respectively). Linear trends are also presented (red color lines) together with their respective equations per simulation period

Table 7 MODSUR model results of (A) River Discharge RD (m^3/s), (B) respective differences Diff (%) between climatic scenario runs, and (C) Diff (%) by different forcing input as CMCC-, CNRM-, and GUF-forced hydrologic implementations. Explanation of Diff in description of Table 4

Study case		A			B			C		
Scenario	Period	CMCC MODSUR *RD* (m^3/s)	CNRM MODSUR *RD* (m^3/s)	GUF MODSUR *RD* (m^3/s)	CMCC MODSUR Diff (%)	CNRM MODSUR Diff (%)	GUF MODSUR Diff (%)	CMCC-CNRM MODSUR Diff (%)	CNRM-GUF MODSUR Diff (%)	GUF-CMCC MODSUR Diff (%)
Historical	RP	73.50	60.41	54.31	0	0	0	19.56	10.63	– 30.03
RCP4.5	STF	72.18	62.37	24.78	– 1.80	3.25	– 54.38	14.58	86.28	– 97.78
RCP4.5	LTF	61.70	61.52	27.01	– 16.06	1.84	– 50.27	0.29	77.97	– 78.21
RCP8.5	STF	78.32	56.77	20.44	6.55	– 6.03	– 62.36	31.91	94.08	– 117.20
RCP8.5	LTF	37.85	51.41	14.97	– 48.50	– 14.90	– 72.44	– 30.37	109.80	– 86.66

a decrease that varies between – 54.38 and – 62.36%. The simulations based on the latter climate model also show a very large decrease of – 72.44% of the river discharges for 2071–2100 (LTF period) under the RCP8.5 approach. For the specific climatic scenario both simulations based on the CMCC and CNRM datasets exhibit a future decrease of the river runoff of – 48.5% and – 14.9% respectively. Table 7 also highlights the percentage differences between the simulated discharges per driving climatic model, RCP and period of simulation. More importantly, the outputs triggered by the GUF model present the higher deferrization in comparison to the simulated discharges forced by the other two RCMs. For example, in the case of RCP8.5 and STF period, the GUF-forced simulations vary by 117.2% and 94.08% in comparison with the discharges simulated when the CMCC and CNRM models are used as forcing inputs of MODSUR.

5.4 Water Demand Coverage

The WEAP model, forced by MODSUR for river discharge data, using GUF, CMCC, and CNRM precipitation and temperature data to calculate water demand (Eqs. 4–7), is applied for each RCM, RCP, WCS, and simulation period. The outputs of the WEAP model refer to the unmet demand of agricultural water needs within the delta as well as the probability of water deficit occurrence. Based on the model results, irrigation water deficit is observed for the RCP8.5 scenario of the GUF model for the LTF period and only by WCS-REF and WCS-EXT implementations. In these two cases, irrigation water demands are not fully covered for 6 and 5 years (out of 30 simulated), respectively. The related deficit corresponds on average to 8797 ha and 14,450 ha, namely 44% and 72% of total agricultural land, with a corresponding deficit probability of 20% and 17%, respectively. The operation of the two hydropower plants and their reservoirs' storage capacity play a significant role in controlling potential water deficit situations. It was observed

Table 8 Thermal stress assessment results of HT probability, HTP (%), for each climatic scenario/period by different climatic data series from CMCC, CNRM, and GUF

Scenario	Period	CMCC *HTP* (%)	CNRM *HTP* (%)	GUF *HTP* (%)
Historical	RP	6.70	0.00	0.00
RCP4.5	STF	26.67	3.33	26.67
RCP4.5	LTF	53.33	16.67	40.00
RCP8.5	STF	43.33	10.00	33.33
RCP8.5	LTF	80.00	30.00	70.00

that even in dry years, the stocked water in the reservoirs fulfilled that year's water demands and only in sequenced dry years, e.g., for the GUF/RCP8.5 future climate, the downstream demands were not met.

5.5 High-Temperature Stress Assessment

According to the analysis of daily temperature data from all RCMs, RCPs, and time periods, only maize cultivation is predicted to be affected due to HT stress. The thermal stress affected area is expected to be 7424 ha in the cases of WCS-REF and WCS-CC and 11,137.2 ha if the current irrigation network is expanded (WCS-EXT). The relevant probability of HT occurrence, *HTP* (%), namely the number of years of thermal stress per tricennial, has been calculated and is presented in Table 8.

Based on CNRM temperature estimations, the *HTP* is lower (compared with CMCC and GUF) in all RCPs and time periods. The highest probabilities are observed in the second half of the twenty-first century (LTF), under RCP8.5 based on GUF and CMCC temperature data. Specifically, heat stress is expected for 21 and 24 years of the tricennial, for the GUF and CMCC data cases, respectively.

Integrated Deltaic Risk Index

The IDRI consists of the coupling of three individual indexes, namely CFRI, WSRI, and HSRI, for coastal flooding, water scarcity and heat stress, respectively. Figure 12 presents the produced risk matrices for each individual index as well as the integrated one. The five-classes ranking defines the severity of probable hazards related to storm surge-driven coastal inundation, water scarcity, high temperature, and their coupled impacts (IDRI) within the deltaic area. Overall, 36 cases are shown for the two 30-year periods of the twenty-first century.

Regarding the individual indexes, coastal inundation risk (CFRI) is expected to peak in the first half of the

a) Coastal Flood Risk Index

SCENARIO \ PERIOD		STF: 2021-2050			LTF: 2071-2100		
RCP	RCM \ WCS	REF	CC	EXT	REF	CC	EXT
4.5	CMCC	1	1	1	1	1	1
	CNRM	1	1	1	1	1	1
	GUF	5	5	5	3	3	3
8.5	CMCC	2	2	2	1	1	1
	CNRM	2	2	2	1	1	1
	GUF	3	3	3	2	2	2

b) Water Scarcity Risk Index

SCENARIO \ PERIOD		STF: 2021-2050			LTF: 2071-2100		
RCP	RCM \ WCS	REF	CC	EXT	REF	CC	EXT
4.5	CMCC	1	1	1	1	1	1
	CNRM	1	1	1	1	1	1
	GUF	1	1	1	1	1	1
8.5	CMCC	1	1	1	1	1	1
	CNRM	1	1	1	1	1	1
	GUF	1	1	1	4	1	5

c) Heat Stress Risk Index

SCENARIO \ PERIOD		STF: 2021-2050			LTF: 2071-2100		
RCP	RCM \ WCS	REF	CC	EXT	REF	CC	EXT
4.5	CMCC	2	2	2	3	3	4
	CNRM	1	1	1	1	1	2
	GUF	2	2	2	2	2	3
8.5	CMCC	2	2	3	4	4	5
	CNRM	1	1	1	2	2	2
	GUF	2	2	3	3	3	5

d) Integrated Deltaic Risk Index

SCENARIO \ PERIOD		STF: 2021-2050			LTF: 2071-2100		
RCP	RCM \ WCS	REF	CC	EXT	REF	CC	EXT
4.5	CMCC	2	2	2	2	2	2
	CNRM	1	1	1	1	1	2
	GUF	3	3	3	2	2	3
8.5	CMCC	2	2	2	2	2	2
	CNRM	2	2	2	2	2	2
	GUF	2	2	3	3	2	4

RISK INDEX		
Rank	Class	Color
VERY LOW	1	
LOW	2	
MODERATE	3	
HIGH	4	
VERY HIGH	5	

Fig. 12 Risk matrices for **a** CFRI, **b** WSRI, **c** HSRI, and **d** IDRI. Climate change impact identification is helped by graphing the differences in color scaling for each risk index, per: water consumption scenario (WCS: REF, CC, EXT), climate modeling input (RCM) for all hydrologic, hydraulic, and hydrodynamic models, Climate change scenario (RCP), and study period (STF, LTF). Thirty-six cases are given in total for the two 30-year periods of the twenty-first century

twenty-first century, especially pronounced for the GUF-driven datasets (very high to moderate for RCP4.5 and 8.5, respectively), while it seems to decrease towards 2100 (Fig. 12a). Regarding WSRI, water scarcity phenomena, in terms of surface water availability for irrigation, are estimated to have a high to very high risk of occurrence, again for GUF-driven data of 2071–2100, under two WCS, namely REF and EXT, where the irrigation demands on water are not expected to be fully covered for 6 and 5 years (out of 30), respectively (Fig. 12b). Regarding HSRI, a more diverse pattern of future risk assessment can be observed. High temperatures are more likely to occur towards the end of the twenty-first century for the CMCC and GUF RCMs, and more pronounced under the RCP8.5 scenario, reaching from high up to very high risks especially in the WCS-EXT framework (Fig. 12c). The integrated index, IDRI, ranges between very low to low, in the cases of the CNRM and CMCC climatic data regardless of the selected WCS (Fig. 12d). This is attributed to the higher mean annual precipitation and the lower temperature during the summer period compared with the corresponding GUF model variables, where moderate impact is expected both in STF and LTF under the RCP4.5 scenario. High risk is estimated to be exerted on the natural environment and related human activities at the Nestos river delta in the last thirty years of the twenty-first century, only for the case of the GUF model and the RCP8.5 scenario under the WCS-EXT (Fig. 12d). In most examined cases, this pressure is exclusively attributed to high temperature stress and water deficit occurrence (Fig. 12b, c) rather than coastal inundation. The risk of the latter is expected to be very high under GUF-driven RCP4.5 scenario realization (Fig. 12a).

6 Discussion

The vulnerability of the Nestos river's delta due to climate change was investigated within the present research. To do so, the implementation of an Integrated Drought Risk Index was proposed that couples the estimated future river discharges and relevant hydropower dam operation, the potential storm-induced coastal floods, and the projected high temperature stress to the cultivations. The irrigation water demands estimation inside the delta was based on the current situation, i.e., a horizontal water demand regardless the cultivation type, and on an adaptive escalator methodology, for which the demands on water are estimated based on sustainable irrigation practices under the future climatic conditions. The literature demonstrates studies proposing coupled or de-coupled applications of maritime hydrodynamic circulation and river hydrology simulations for current and future climate change conditions. Nevertheless, these studies put emphasis mainly on the sea water intrusion within the river's main course and the coastal aquifers [93–97]. However, to the authors' knowledge, the presently proposed indexing of concomitant hydrodynamic (coastal waters), hydrologic (river waters), and hydraulic (dam operation) outputs for the study of deltaic areas' vulnerability in terms of irrigated agriculture under climate change is rather limited.

6.1 Deltaic Vulnerability and Risk Indexing Issues

The presented outputs let us infer that the proposed sustainable irrigation practices in deltas are appropriate measures for adaptation to climate change and are in line with the literature [98]. Practically, it is concluded that if rational water use measures are applied locally in agriculture, the water reserves of the study area are sufficient to meet irrigation needs both in the short- and long-term future. Investment actions in the Greek farming sector (e.g., irrigation network expansion) could partially be implemented in the Nestos river delta, depending on the climate change scenario. Thus, agriculture adaptation strategies are mandatory managerial actions to ensure environmental sustainability and socio-economic development for the study area. These refer to the evaluation of agricultural patterns, the restructuring of crops in the context of climate change, and the transition to crops highly resistant to temperature stress. Vermeulen et al. [99] demonstrate various case studies around the world where agricultural shifts due to climate change are conducted. Nevertheless, Iglesias and Garrote [100] reviewed 168 publications on adaptation strategies and concluded that the transition to sustainable agriculture is not a straightforward procedure. Its implementation requires the enhancement of the current water policy, adequate training to farmers and strong financial instruments. We have studied the risks of three regionally important processes (namely CFRI, WSRI, HSRI) as the crucial manifestations of local natural and anthropogenic hazards in the study region. The estimation of the related risk indices helps us to compose the integrated risk in deltaic areas according to Eq. 8, for each WCS (REF, CC, EXT), RCP scenario (4.5 and 8.5), available climatic input (CNRM, GUF, CMCC) forcing all implemented models (MeCSS, CoastFLOOD, MODSUR, and WEAP), and study period (RP, STF, LTF). Thus, 39 implementations in total have been conducted (see Fig. 1). In terms of coastal inundation, the flood impact is expected to be low in the cases of CNRM- and CMCC-driven climate conditions and moderate to very high in the case of the GUF model projected climate. However, only a few coastal-related economic activities seem to be affected in all 39 cases (Figs. 2

and 9). Despite the projected decrease of the river runoff, the water scarcity also poses limited significant threat for the river's delta only for specific scenarios. This is mainly due to the two large reservoirs of the hydropower dams that are located upstream of the delta. Vano et al. [101] demonstrate that by changing reservoir operation rules and allowing larger flows to water users, the climate change impacts may be reduced. On the other hand, based on stakeholders' responses for a Spanish basin, Varela-Ortega et al. [98] demonstrated that public-funded hard adaptation measures, such as the increase of reservoirs' storage capacity, has the lower public acceptance in comparison to the measure of sustainable agriculture that was the first priority of the stakeholders. However, as proposed by Hallegate [102], the coupling of structural and nonstructural measures is often required to efficiently reduce the impacts of climate change.

The diversity of IDRI hinges on heat stress assessment, as the main cultivation (maize) within the delta is expected to be significantly affected by the estimated dramatic temperature increase, especially during the period 2071–2100. HT impact on maize crop yield is a major concern among the scientific community. Taoyuan et al. [103] statistically estimated the impact of heat waves (and other extreme events) on maize yield, based on household survey data from 1993 to 2011 in ten villages of Shanxi province, China, demonstrating marginal yield declines for the study period. However, in climate change conditions as derived by six climate models and two future climate forcing scenarios, Hong [104] presented a decrease in maize yield ranging from 15 to 50%. Our findings show that the HT probability (*HTP* in Table 8) for the RCP8.5 was estimated up to 80% and 70% for the CMCC and GUF climate models, respectively.

6.2 RCM Forcing and Modelling Issues of Projected Climate Change Impact

We consider the use of a plethora of climatic parameters' input by three different RCMs and two RCPs, as an important asset in assessing the vulnerability of the case study deltaic area. The specific approach coincides with the latest research concerning climate change effects on water resources, irrigated agriculture, and coastal hydrodynamics [15, 105]. In particular, the single RCM approach is not advised, due to known climate model bias, in addition to other sources of uncertainties in the modeling chain. Instead, ensembles of RCM simulation results, i.e., combinations of various models and scenarios, should be used [106].

The utilized RCMs play an important role to the research outputs [105]. In our case, it was shown that the future river discharges could vary up to 117.20% and 97.78% for the RCP8.5 and RCP4.5, respectively, among the different hydrologic simulations triggered by three RCM data series (Table 7). The main reason behind these variations is related to the accuracy of hindcast precipitation and temperature data provided by the RCMs feeding hydrologic modeling. Pavlidis et al. [56] correlated the summer temperature and precipitation variables from six climate models covering the EURO-CORDEX domain, amongst them the CNRM and CMCC, with E-OBS datasets for the period 1990–2008. They concluded that the temperature bias is negligible, while the modelled precipitation is overestimated, compared with the E-OBS data. Lazoglou et al. [75] compared daily precipitation data from 1980 to 2000 derived from three stations at the boundaries of the Mesta/Nestos river basin, i.e., the same case study area with the current research, with spatiotemporal relevant hindcast precipitation data coming from the regional climate model of the Max Plank Institute (MPI). In all stations, the MPI model's precipitation was highly overestimated, with the correlation index to vary between 0.2 and 0.39, thus the necessity of bias correction techniques on precipitation to be proposed. In this research, the CNRM and CMCC bias corrected precipitation remained overestimated in comparison to the in situ data. The GUF bias corrected precipitation was well correlated with the in situ precipitation, apart from the 1988–1994 period, which was a designated dry period for the area. The observed differentiations of the hindcast and observed precipitation are passed on the simulated RP discharges, as depicted in Fig. 7. In general, the RP simulated outputs are used as incipient data for scenario simulations in the twenty-first century; thus, the produced future climatic variable fluctuations will be less severe, if they are based on overvalued initial conditions [107].

The presented results clearly demonstrate variabilities following the differentiations of the three RCMs used to trigger the hydrologic and hydrodynamic model simulations. Particularly, in RCP4.5-forced future projections, the standard deviation among the averaged simulated river discharges at the delta's neck is 25.02 m^2/s and 19.98 m^2/s for the STF and LTF periods, respectively. For the RCP8.5-forced future hydrologic projections, the deviation among the averaged simulated river discharges is 29.25 m^2/s and 18.4 m^2/s for the STF and LTF periods, respectively. A significant decrease of 24.8% of the Nestos river runoff entering Greece, in comparison with the control data period, is also mentioned by Skoulikaris and Ganoulis [77] for the SRES-B1 climatic scenario in the same basin.

In terms of maritime and coastal hydrodynamics, we note that previous works [33–35] using the 20C3M historical dataset and SRES-A1B future scenario, are corroborated by the RCP-forced storm surge simulations. The highest *SSI* values in the Mediterranean region occur over the northern Aegean coastal region (Alexandroupoli), where both modelled and observed *SSI* are higher than 23 cm for all

implementations. Even though the model underestimates the *SSI* at the chosen check-point station (negative *EI* values), the error is generally acceptable and differences between SSI_{mod} and SSI_{obs} values are plausible. However, both model results and observations show rather low *SSI* values (< 40 cm), supporting the low presence of *SSH* extremes in the study area due to meteorological forcing. Conte and Lionello [32] have also shown results of climate storm surge simulations with significantly high errors *E* (> 40%) and similar underestimations of the simulated *SSH* over various coastal regions of the Mediterranean. The integrated RMSE for the entire *SSH* time series in all simulations is equal to 0.04 m, which gives a RMSE/SSH_{max} ratio of 13.5% (acceptable in climatic studies).

Even though the MeCSS model slightly underestimates the magnitude of extreme surges, it performs well in terms of predicting the frequency of occurrence of local maxima in its timeseries (not shown herein for the sake of brevity) and other probabilistic features of *SSH* maxima. In general, the differences in probabilistic features of storm surge levels produced by MeCSS simulations are marginal and not able to offer a definite reason for discarding the one or the other model setup (either RCM/RCP used as forcing input). Generally, it can be concluded that MeCSS model can adequately reproduce the probabilities of occurrence and the maximum values of storm surge levels, as well as their flood-inducing patterns. Thus, the statistical distributions of the modelled *SSH* data were reliable for further use in inundation modeling and flood risk assessment in terms of the deltaic vulnerability analysis presented herein. Conclusively, model to field data comparisons show acceptable agreement, thus we can confirm the ability of MeCSS model to estimate the response of the sea surface elevation to historical and future climatic conditions.

The CoastFLOOD module is a rather simplistic approach for coastal flood modeling but seems to adequately reproduce long-lasting steady-state inundation events. It is considered able to provide rather conservative, yet plausible, estimates of inundated areas under saturated flood conditions for storm surges. This way the necessary numerical modeling was completed in a time-affordable manner with the available computational processing resources. Various model runs of 15 discrete climatic mode implementations were conducted on a very high spatial resolution domain. The simulated inundated areas cover a 19.4 to 25.1% of the potentially flooded low-land area under extreme conditions [69]. CMCC- and GUF-forced simulations in the study region for the twenty-first century, under any RCP scenario, have produced results that confirm a tendency towards storminess attenuation. The latter is indicated by a decrease factor of − 2 to − 14% for storm surge levels and − 8 to − 20% for coastal inundation extends, respectively. However, based on CNRM-forced MeCSS-CoastFLOOD results, the storm surge and flooded coastal areas maxima in the Nestos river delta are estimated to increase up to 9% and 6.5%, respectively, for both scenarios in the twenty-first century compared with the past. In general, storminess and related coastal flooding by surges is expected to further decrease towards the end of the twenty-first century compared with the 2021–2050 period. This is the case for most of the combinations of RCP-scenario to hydrodynamic model implementation. Additional impacts of wave-induced run-up or MSL rise, due to steric effects, on coastal flooding, under climate change conditions, were not considered in the present study. This is set as a future goal of research.

6.3 Bias Corrections of Future Climate Projections and Water Management Proposals

Issues that could further be enhanced are related with the proposed bias correction method and the operation rules of the hydropower dams' simulation model. Regarding bias correction of RCM reference data, the lack of daily precipitation records, mainly in the upstream Bulgarian part of the basin, was a deteriorative factor. The implemented method has the advantage of simplicity and modest data requirements, i.e., monthly climatological information, while its efficiency is well documented [108]. However, correcting only the monthly mean precipitation could distort the relative variability of the inter-monthly precipitation distribution and may adversely affect other moments of the probability distribution of daily precipitations [109].

The second issue has to do with the operational rules of the WEAP model when the simulation of the dams is conducted. In this paper, the ultimate priority was the maintenance of the environmental flow of 6.0 m^3/s, followed by the coverage of the irrigation demands and the electrical power production, designated as the last priority. The reservoirs were thus not calibrated to consider potential wet seasons, i.e., to attenuate the outflows that are oriented to environmental flows and agriculture in favor of hydropower production. More sophisticated approaches implementing optimization techniques for the reservoirs' operation could be further used for the overall management of the hydrosystem [110].

To sum up, with the proposed research, the authors' aspiration was to promote a practical combination of various models representing different domains, i.e., coastal zone, inland waters, hydropower infrastructure, and agricultural plains, focusing on deltaic environments under the scope of vulnerability assessment. The proposed index, namely IDRI, demonstrates the importance of integrated approaches, since by considering the risks via stand-alone processes, e.g., solely the risk of coastal flooding and the relevant CFRI, the deltaic vulnerability is importantly underestimated than in the case of the integrated risk index. Moreover, the procedure of intercorrelating disparate processes, such as coastal

flooding with agricultural heat stress and river hydrology, is considered an asset of the proposed IDRI approach, as it induces novel management application locally in deltaic areas allowing for relatively effortless implementation in other similar case study areas. The pursuit of further research enhancement lies in the socioeconomic assessment of the identified impacts and the integration of a multicriteria approach in the framework of an easy-to-use decision support model. This could assist in identifying optimal solutions in a complex multi-parametric environment, under a variety of natural and anthropogenic pressures. Apart from quantifying the impact, a holistic assessment of the hydrosystem, in the context of the water-energy-food-environment nexus, is also planned to be applied soon.

7 Conclusions

Combining data from various coastal and land water related models to an Integrated Deltaic Risk Index was proposed as a conceptual approach to monitor the impact of climate change to the coastal zone, surface waters, and irrigated agriculture at a Mediterranean deltaic environment. The principal aim was to focus on coastal inundation, river hydrology, dam operation, water scarcity, and high temperature stress on irrigated agriculture. A wide range of parameters, i.e., sea surface height, coastal flooded areas, river discharges, water budget, precipitation, and summer temperature parameters, was assessed to investigate the Nestos river delta's vulnerability and its response to climate change. The results show that climate impact will remain in relatively low levels in most of the cases under study. However, the major threat is expected in the last 30 years of the twenty-first century, where cases of severe temperature increase, and precipitation decrease is projected. Due to the two large reservoirs in the hydrosystem, water scarcity phenomena will not be observed if rational and sustainable water use in agriculture is applied. On the other hand, temperature stress and coastal inundation are estimated to have more radical impacts on the deltaic area under certain probable future climate projections. Furthermore, in terms of socioeconomic impact, touristic economic activities on the coastal zone are not expected to be affected by flood events, whereas the environmental impacts on the protected areas and the nearby agriculture could be important.

We consider the presented CCI identification method based on coupled risk assessment for deltaic areas to be significant, as our approach follows an integrated vision dealing with issues that have important social, economic, and environmental repercussions, i.e., impacts on the water-energy-food-environment nexus under several possible realizations of projected future climate change. In particular, the presented research effort will hopefully allow to (a) achieve sustainable development regionally, (b) meet the actual needs of local inhabitants of coastal zones especially those suffering from scarcity of water and climate change related hazards, (c) improve the environmental context by the added value of water resources management and control, and (d) render the local authorities and water resources professionals (managers, planners, and engineers) in the study area as immediate beneficiaries.

Authors' Contributions Conceptualization: Charalampos Skoulikaris, Christos Makris, Margarita Katirtzidou, Vasilios Baltikas, Yannis Krestenitis; methodology: Charalampos Skoulikaris, Christos Makris, Margarita Katirtzidou; formal analysis and investigation: Charalampos Skoulikaris, Christos Makris, Margarita Katirtzidou, Vasilios Baltikas; writing—original draft preparation: Charalampos Skoulikaris, Christos Makris, Margarita Katirtzidou; writing—review and editing: Charalampos Skoulikaris, Christos Makris; funding acquisition: Yannis Krestenitis; resources: Charalampos Skoulikaris, Christos Makris, Margarita Katirtzidou, Vasilios Baltikas; supervision: Charalampos Skoulikaris, Yannis Krestenitis.

Funding This research is part of the MEDAQCLIM project: *Integrated Quantitative Assessment of Climate Change Impacts on Mediterranean Coastal Water Resources and Socioeconomic Vulnerability Mapping*, which is financed by the National Action Plan: "European R&D Cooperation—Grant Act of Greek partners successfully participating in Joint Calls for Proposals of the European Networks ERA-NETS" and the "Competitiveness, Entrepreneurship & Innovation" Program.

Data Availability The level of research datasets/material dissemination is set to "Confidential among Project Partners" within MEDAQCLIM Project, therefore data are not publicly accessible, but may be shared by the authors upon official request.

References

1. Ericson, J. P., Vörösmarty, C. J., Dingman, S. L., Ward, L. G., & Meybeck, M. (2006). Effective sea-level rise and deltas: causes of change and human dimension implications. *Global and Planetary Change, 50*(1–2), 63–82.
2. Pont, D., Day, J. W., Hensel, P., Franquet, E., Torre, F., Rioual, P., et al. (2002). Response scenarios for the deltaic plain of the Rhône in the face of an acceleration in the rate of sea-level rise with special attention to Salicornia-type environments. *Estuaries, 25*(3), 337–358.
3. Kuenzer, C., & Renaud, F. G. (2012). Climate and environmental change in river deltas globally: expected impacts, resilience, and adaptation. In F. Renaud, C. Kuenzer (Ed.) *The Mekong Delta System*. Springer Environmental Science and Engineering, Dordrecht.
4. Adger, W. N. (2018). Ecosystem services, well-being and deltas: current knowledge and understanding. In R. Nicholls, et al. (Ed.) *Ecosystem services for well-being in deltas*. Palgrave Macmillan, Cham.
5. Zhong, S., et al. (2019). Analyzing ecosystem services of freshwater lakes and their driving forces: the case of Erhai Lake, China. *Environmental Science and Pollution Research, 26,* 10219–10229.
6. Szabo, S., et al. (2016). Population dynamics, delta vulnerability and environmental change: comparison of the Mekong, Ganges-Brahmaputra and Amazon delta regions. *Sustainability Science, 11,* 539–554.

7. Lionello, P., & Scarascia, L. (2018). The relation between climate change in the Mediterranean region and global warming. *Regional Environmental Change, 18*(5), 1481–1493.
8. Cramer, W., et al. (2018). Climate change and interconnected risks to sustainable development in the Mediterranean. *Nature Climate Change, 8*(11), 972–980.
9. Allen, M. R., Barros, V. R., Broome, J., Cramer, W., Christ, R., Church, J. A., Clarke, L., Dahe, Q., Dasgupta, P., Dubash, N. K., & Edenhofer, O. (2014). *IPCC Fifth Assessment Synthesis Report Climate Change 2014 Synthesis Report.*
10. Makarigakis, A. K., & Jimenez-Cisneros, B. E. (2019). UNESCO's contribution to face global water challenges. *Water, 11,* 388.
11. Boone, R. B., Conant, R. T., Sircely, J., Thornton, P. K., & Herrero, M. (2018). Climate change impacts on selected global rangeland ecosystem services. *Global Change Biology, 24*(3), 1382–1393.
12. Iglesias, A., Mougou, R., Moneo, M., & Quiroga, S. (2011). Towards adaptation of agriculture to climate change in the Mediterranean. *Regional Environment Change, 11*(1), 159–166.
13. Mollema, P., Antonellini, M., Gabbianelli, G., Laghi, M., Marconi, V., & Minchio, A. (2012). Climate and water budget change of a Mediterranean coastal watershed, Ravenna Italy. *Environmental Earth Sciences, 65*(1), 257–276.
14. Faysse, N., et al. (2014). Participatory analysis for adaptation to climate change in Mediterranean agricultural systems: possible choices in process design. *Regional Environmental Change, 14*(1), 57–70.
15. Ronco, P., Zennaro, F., Torresan, S., Critto, A., Santini, M., Trabucco, A., et al. (2017). A risk assessment framework for irrigated agriculture under climate change. *Advances in Water Resources, 110,* 562–578.
16. Ahuja, I., de Vos, R. C. H., Bones, A. M., & Hall, R. D. (2010). Plant molecular stress responses face climate change. *Trends in Plant Science, 15,* 664–674.
17. McClung, C. R., & Davis, S. J. (2010). Ambient thermometers in plants: from physiological outputs towards mechanisms of thermal sensing. *Current Biology, 20,* 1086–1092.
18. Lobell, D. B., Schlenker, W., & Costa-Roberts, J. (2011). Climate trends and global crop production since 1980. *Science, 333,* 616–620.
19. Hasanuzzaman, M., Nahar, K., Alam, Md., Roychowdhury, R., & Fujita, M. (2013). Physiological, biochemical, and molecular mechanisms of heat stress tolerance in plants. *International Journal of Molecular Sciences, 14*(5), 9643–9684.
20. Masia, S., Sušnik, J., Marras, S., Mereu, S., Spano, D., & Trabucco, A. (2018). Assessment of irrigated agriculture vulnerability under climate change in Southern Italy. *Water, 10,* 209.
21. Wang, X., Zhang, J., Ali, M., Shahid, S., He, R., Xia, W., & Jiang, Z. (2016). Impact of climate change on regional irrigation water demand in Baojixia irrigation district of China. *Mitigation and Adaptation Strategies for Global Change, 21,* 233–247.
22. Riediger, J., Breckling, B., Svoboda, N., & Schröder, W. (2016). Modelling regional variability of irrigation requirements due to climate change in Northern Germany. *Science of the Total Environment, 541,* 329–340.
23. Allen, R. G., Pereira, L. S., Raes, D., & Smith, M. (1998). Crop evapotranspiration - guidelines for computing crop water requirements-FAO Irrigation and drainage paper 56. *FAO, Rome, 300*(9), D05109.
24. Jiří, M. L. S. (1980). Effective rainfall estimation. *Journal of Hydrology, 45*(3–4), 305–311.
25. FAO. (1986). Irrigation water management: irrigation water needs. Training manual 3, Food and Agriculture Organization of the United Nations, Rome, Italy.
26. Kew, S. F., Selten, F. M., Lenderink, G., & Hazeleger, W. (2013). The simultaneous occurrence of surge and discharge extremes for the Rhine delta. *Natural Hazards and Earth System Sciences, 13*(8), 2017–2029.
27. Auerbach, L. W., Goodbred, S. L., Jr., Mondal, D. R., Wilson, C. A., Ahmed, K. R., Roy, K., et al. (2015). Flood risk of natural and embanked landscapes on the Ganges-Brahmaputra tidal delta plain. *Nature Climate Change, 5*(2), 153.
28. Oude Essink, G. H. P., Van Baaren, E. S., De Louw, P. G. (2010). Effects of climate change on coastal groundwater systems: a modeling study in the Netherlands. *Water Resour Res*, *46*(10).
29. Sánchez-Arcilla, A., Mösso, C., Sierra, J. P., Mestres, M., Harzallah, A., Senouci, M., & El Raey, M. (2011). Climatic drivers of potential hazards in Mediterranean coasts. *Regional Environmental Change, 11*(3), 617–636.
30. Jordà, G., Gomis, D., Álvarez-Fanjul, E., & Somot, S. (2012). Atmospheric contribution to Mediterranean and nearby Atlantic sea level variability under different climate change scenarios. *Global and Planetary Change, 80,* 198–214.
31. Calafat, F. M., Jordà, G., Marcos, M., & Gomis, D. (2012). Comparison of Mediterranean sea level variability as given by three baroclinic models. *Journal of Geophysical Research, 117,* C02009.
32. Conte, D., & Lionello, P. (2013). Characteristics of large positive and negative surges in the Mediterranean Sea and their attenuation in future climate scenarios. *Global and Planetary Change, 111,* 159–173.
33. Androulidakis, Y., Kombiadou, K., Makris, C., Baltikas, V., & Krestenitis, Y. (2015). Storm surges in the Mediterranean Sea: variability and trends under future climatic conditions. *Dynamics Atmospheres and Oceans, 71,* 56–82.
34. Makris, C. V., Androulidakis, Y. S., Krestenitis, Y. N., Kombiadou, K. D., Baltikas, V. N. (2015). Numerical modelling of storm surges in the Mediterranean sea under climate change. Proc 36th IAHR World Cong, The Hague, The Netherlands.
35. Makris, C., et al. (2016). Climate change effects on the marine characteristics of the Aegean and the Ionian seas. *Ocean Dynamics, 66*(12), 1603–1635.
36. Galiatsatou, P., Makris, C., Prinos, P., & Kokkinos, D. (2019). Nonstationary joint probability analysis of extreme marine variables to assess design water levels at the shoreline in a changing climate. *Natural Hazards, 98,* 1051–1089.
37. Marcos, M., Rohmer, J., Vousdoukas, M. I., Mentaschi, L., Le Cozannet, G., & Amores, A. (2019). Increased extreme coastal water levels due to the combined action of storm surges and wind waves. *Geophysical Research Letters, 46*(8), 4356–4364.
38. Kaniewski, D., Marriner, N., Morhange, C., Faivre, S., Otto, T., & Van Campo, E. (2016). Solar pacing of storm surges, coastal flooding and agricultural losses in the Central Mediterranean. *Scientific Reports, 6,* 25197.
39. Paprotny, D., Vousdoukas, M. I., Morales-Nápoles, O., Jonkman, S. N., & Feyen, L. (2020). Pan-European hydrodynamic models and their ability to identify compound floods. *Natural Hazards, 101*(3), 933–957.
40. Sudha Rani, N. N. V., Satyanarayana, A. N. V., & Bhaskaran, P. K. (2015). Coastal vulnerability assessment studies over India: a review. *Natural Hazards, 77,* 405–428.
41. Ramieri, E., Hartley, A., Barbanti, A., Santos, F., Gomes, A., Hildén, M., et al. (2011). Methods for assessing coastal vulnerability to climate change. *ETC CCA Technical Paper, 1*(2011), 1–93.
42. Gornitz, V. (1990). Vulnerability of the East Coast, USA to future sea level rise. *Journal of Coastal research*, 201–237.
43. Balica, S. F., Wright, N. G., & van der Meulen, F. (2012). A flood vulnerability index for coastal cities and its use in assessing climate change impacts. *Natural Hazards, 64,* 73–105.
44. Torresan, S., Critto, A., Rizzi, J., & Marcomini, A. (2012). Assessment of coastal vulnerability to climate change hazards

at the regional scale: the case study of the North Adriatic Sea. *Natural Hazards and Earth Systems Sciences, 12,* 2347–2368.
45. Satta, A., Snoussi, M., Puddu, M., Flayou, L., & Hout, R. (2016). An index-based method to assess risks of climate-related hazards in coastal zones: the case of Tetouan. *Estuar Coast Shelf S, 175,* 93–105.
46. Mani Murali, R., Ankita, M., Amrita, S., & Vethamony, P. (2013). Coastal vulnerability assessment of Puducherry coast, India, using the analytical hierarchical process. *Natural Hazards and Earth Systems Sciences, 13,* 3291–3311.
47. Pereira, L. S., Cordely, I., & Iacovides, I. (2009). *Coping with water scarcity*. Springer, The Netherlands: Addressing the challenges.
48. Beguería, S., Vicente-Serrano, S. M., Reig, F., & Latorre, B. (2014). Standardized precipitation evapotranspiration index (SPEI) revisited: parameter fitting, evapotranspiration models, tools, datasets and drought monitoring. *International journal of climatology, 34*(10), 3001–3023.
49. Zarch, M. A. A., Sivakumar, B., & Sharma, A. (2015). Droughts in a warming climate: a global assessment of Standardized precipitation index (SPI) and Reconnaissance drought index (RDI). *Journal of Hydrology, 526,* 183–195.
50. Safavi, H. R., Esfahani, M. K., & Zamani, A. R. (2014). Integrated index for assessment of vulnerability to drought, case study: Zayandehrood River Basin Iran. *Water Resources Management, 28,* 1671–1688.
51. Thomas, T., Jaiswal, R. K., & Galkate, R. (2016). Drought indicators-based integrated assessment of drought vulnerability: a case study of Bundelkhand droughts in central India. *Natural Hazards, 81,* 1627–1652.
52. Sönmez, F. K., Kömüscü, A. Ü., & Erkan, A. (2005). An analysis of spatial and temporal dimension of drought vulnerability in Turkey using the standardized precipitation index. *Natural Hazards, 35,* 243–264.
53. Lybbert, T., & Carter, M. (2015). Bundling drought tolerance and index insurance to reduce rural household vulnerability to drought. *Sustainable Economic Development, 22,* 401–414.
54. Skoulikaris, C., & Zafirakou, A. (2019). River basin management plans as a tool for sustainable transboundary river basins' management. *Environmental Science and Pollution Research, 26*(15), 14835–14848.
55. Ruti, P. M., et al. (2016). MED-CORDEX initiative for Mediterranean climate studies. *Bulletin of the American Meteorological Society, 97*(7), 1187–1208.
56. Pavlidis, V., Katragkou, E., Zanis, P., Karacostas, T. S. (2017). Evaluation of summer temperature and precipitation of EURO-CORDEX regional climate simulations. In: T. Karacostas, A. Bais, P. Nastos (Ed.) Perspectives on atmospheric sciences, Springer Atmospheric Sciences. Springer, Cham.
57. Hay, L. E., Wilby, R. L., & Leavesley, G. H. (2000). A comparison of delta change and downscaled GCM scenarios for three mountainous basins in the United States. *Journal of the American Water Resources Association, 36*(2), 387–397.
58. Böhm, U., Gerstengarbe, F. W., Hauffe, D., Kücken, M., Österle, H., & Werner, P. C. (2003). *Dynamic regional climate modeling and sensitivity experiments for the northeast of Brazil* (pp. 153–170). Berlin, Heidelberg: Glob Change Reg Impacts. Springer.
59. Rockel, B., Will, A., & Hense, A. (2008). The regional climate model COSMO-CLM (CCLM). *Meteorologische Zeitschrift, 17*(4), 347–348.
60. Radnóti, G., et al. (1995). The spectral limited area model ARPEGE/ALADIN. *PWPR Report Series, 7,* 111–117.
61. Madec, G., et al. (2012). NEMO ocean engine. *Note du Pole de modélisation de l'Institut Pierre-Simon Laplace, France, 27,* 1288–1619. In French.
62. De Vries, H., Breton, M., de Mulder, T., Krestenitis, Y., Proctor, R., Ruddick, K., et al. (1995). A comparison of 2D storm surge models applied to three shallow European seas. *Environ Softw, 10*(1), 23–42.
63. Krestenitis, Y., Androulidakis, Y., Kombiadou, K., Makris, C., Baltikas, V. (2014). Modeling storm surges in the Mediterranean Sea under the A1B climate scenario. *Proc 12*th *Int Conf Meteorol, Climatol Atm Phys (COMECAP), Heraklion (Crete), Greece*, pp. 91–95. Part of ISBN: 978–960–524–430–9.
64. Krestenitis, Y., Makris, C., Androulidakis, Y., Kombiadou, K., Baltikas, V. (2015.) Variability of storm surge extremes in the Greek seas under climate change. Proc 2015 ASLO Aquatic Science Meeting, Granada, Spain.
65. Krestenitis, Y., et al. (2017). Severe weather events and sea level variability over the Mediterranean Sea: the WaveForUs operational platform. In T. Karacostas, A. Bais, & P. Nastos (Eds.), *Perspectives on atmospheric sciences, Springer Atmospheric Sciences* (pp. 63–68). Cham: Springer.
66. Bates, P. D., Dawson, R. J., Hall, J. W., Horritt, M. S., Nicholls, R. J., Wicks, J., & Hassan, M. (2005). Simplified two-dimensional numerical modelling of coastal flooding and example applications. *Coastal Engineering, 52*(9), 793–810.
67. Hunter, N. M., Horritt, M. S., Bates, P. D., Wilson, M. D., & Werner, M. G. (2005). An adaptive time step solution for raster-based storage cell modelling of floodplain inundation. *Advance in Water Resources, 28*(9), 975–991.
68. Bates, P. D., Horritt, M. S., & Fewtrell, T. J. (2010). A simple inertial formulation of the shallow water equations for efficient two-dimensional flood inundation modelling. *Journal of Hydrology, 387*(1–2), 33–45.
69. Neal, J., Schumann, G., Fewtrell, T., Budimir, M., Bates, P., & Mason, D. (2011). Evaluating a new LISFLOOD-FP formulation with data from the summer 2007 floods in Tewkesbury UK. *Journal of Flood Risk Management, 4*(2), 88–95.
70. Seenath, A., Wilson, M., & Miller, K. (2016). Hydrodynamic versus GIS modelling for coastal flood vulnerability assessment: Which is better for guiding coastal management? *Ocean Coast Manage, 120,* 99–109.
71. Brufau, P., García-Navarro, P., & Vázquez-Cendón, M. E. (2004). Zero mass error using unsteady wetting–drying conditions in shallow flows over dry irregular topography. *International Journal for Numerical Methods in Fluids, 45*(10), 1047–1082.
72. Castro, M. J., Ferreiro, A. F., García-Rodríguez, J. A., González-Vida, J. M., Macías, J., Parés, C., & Vázquez-Cendón, M. E. (2005). The numerical treatment of wet/dry fronts in shallow flows: application to one-layer and two-layer systems. *Mathematical and Computer Modelling, 42*(3–4), 419–439.
73. Ledoux, E., Girard, G., de Marsily, G., Deschenes, J. (1989). Spatially distributed modelling: conceptual approach, coupling surface water and ground water in unsaturated flow hydrologic modelling—theory and practice. Morel-Seytoux HJ (ed.), *NATO ASI Series S275*, Kluwer Academic: Boston, MA, USA, pp 435–454.
74. Skoulikaris, C., Anagnostopoulou, C., & Lazoglou, G. (2020). Hydrological modeling response to climate model spatial analysis of a South Eastern Europe International Basin. *Climate, 8,* 1.
75. Lazoglou, G., Anagnostopoulou, C., Skoulikaris, C., & Tolika, K. (2019). Bias correction of climate model's precipitation using the copula method and its application in River Basin Simulation. *Water, 11,* 600.
76. Yates, D., Sieber, J., Purkey, D., Huber-Lee, A. (2005a). WEAP21 - a demand-, priority-, and preference-driven water planning model. Part 1: model characteristics. *Water International*, *30*(4): 487–500.

77. Skoulikaris, Ch., & Ganoulis, J. (2017). Multipurpose hydropower projects economic assessment under climate change conditions. *Fresenious Environmental Bull, 26*(9), 5599–5607.
78. Tsoukalas, I., & Makropoulos, C. (2015). A surrogate based optimization approach for the development of uncertainty-aware reservoir operational rules: the case of Nestos hydrosystem. *Water Resources Management, 29*(13), 4719–4734.
79. Yates, D., Purkey, D., Sieber, J., Huber-Lee, A., & Galbraith, H. (2005). Weap21—a demand- priority-, and preference-driven water planning model: part 2: aiding freshwater ecosystem service evaluation. *Water International, 30*(4), 501–512.
80. Hargreaves, G. L., Hargreaves, G. H., & Riley, J. P. (1985). Irrigation water requirements for Senegal River Basin. *Journal of Irrigation and Drainage Engineering, 111*(3), 265–275.
81. Aschonitis, V., Lekakis, E., Tziachris, P., Doulgeris, C., Papadopoulos, F., Papadopoulos, A., & Papamichail, D. (2019). A ranking system for comparing models' performance combining multiple statistical criteria and scenarios: the case of reference evapotranspiration models. *Environmental Modelling and Software, 114,* 98–111.
82. Ebrahimian, A., Wadzuk, B., & Traver, R. (2019). Evapotranspiration in green stormwater infrastructure systems. *Science of the Total Environment, 688,* 797–810.
83. Valle Junior, L. C., Ventura, T., Gomes, R., Nogueira, J., Lobo, D. A., & F., Vourlitis, G., Rodrigues, T. . (2020). Comparative assessment of modelled and empirical reference evapotranspiration methods for a brazilian savanna. *Agricultural Water Management, 232,* 106040.
84. Special Secretariat for Water. (2013). *The river basin management plan of Thrace Water District (GR12)*. Athens, Greece (in Greek): Ministry of Environment and Energy.
85. Edreira, J. I. R., & Otegui, M. E. (2012). Heat stress in temperate and tropical maize hybrids: differences in crop growth, biomass partitioning and reserves use. *Field Crops Research, 130,* 87–98.
86. Suwa, R., et al. (2010). High temperature effects on photosynthetic partitioning and sugar metabolism during ear expansion in maize (Zea mays L.) genotypes. *Plant Physiology and Biochemistry, 48,* 124–130.
87. Rahman, M. A., Chikushi, J., Yoshida, S., & Karim, A. J. M. S. (2009). Growth and yield components of wheat genotypes exposed to high temperature stress under control environment. *Bangladesh Journal of Agricultural Research, 34,* 361–372.
88. Djanaguiraman, M., Prasad, P. V. V., & Al-Khatib, K. (2011). Ethylene perception inhibitor 1-MCP decreases oxidative damage of leaves through enhanced antioxidant defense mechanisms in soybean plants grown under high temperature stress. *Environmental and Experimental Botany, 71,* 215–223.
89. Yin, Y., Li, S., Liao, W., Lu, Q., Wen, X., & Lu, C. (2010). Photosystem II photochemistry, photoinhibition, and the xanthophyll cycle in heat-stressed rice leaves. *Journal of Plant Physiology, 167,* 959–966.
90. Helm, P. (1996). Integrated risk management for natural and technological disasters. *Tephra, 15*(1), 4–13.
91. Carillo, A., Sannino, G., Artale, V., Ruti, P. M., Calmanti, S., & Dell'Aquila, A. (2012). Steric sea level rise over the Mediterranean Sea: present climate and scenario simulations. *Climate Dynamics, 39*(9–10), 2167–2184.
92. Pawlowicz, R., Beardsley, B., & Lentz, S. (2002). Classical tidal harmonic analysis including error estimates in MATLAB using T-TIDE. *Computers & Geosciences, 28,* 929–937.
93. Obeysekera, J., Kuebler, L., Ahmed, S., Chang, M.-L., Engel, V., Langevin, C., et al. (2011). Use of hydrologic and hydrodynamic modeling for ecosystem restoration. *Critical Reviews in Environmental Science and Technology, 41,* 447–488.
94. Yang, Z., Wang, T., Voisin, N., & Copping, A. (2014). Estuarine response to river flow and sea-level rise under future climate change and human development. *Estuarine, Coastal and Shelf Science, 156,* 19–30.
95. Hanington, P., To, Q. T., Van, P. D. T., Doan, N. A. V., & Kiem, A. S. (2017). A hydrological model for interprovincial water resource planning and management: a case study in the Long Xuyen Quadrangle, Mekong Delta Vietnam. *Journal of Hydrology, 547,* 1–9.
96. Wester, S. J., Grimson, R., Minotti, P. G., Booij, M. J., & Brugnach, M. (2018). Hydrodynamic modelling of a tidal delta wetland using an enhanced quasi-2D model. *Journal of Hydrology, 559,* 315–326.
97. Hoch, J. M., Eilander, D., Ikeuchi, H., Baart, F., & Winsemius, H. C. (2019). Evaluating the impact of model complexity on flood wave propagation and inundation extent with a hydrologic-hydrodynamic model coupling framework. *Natural and Hazards Earth System Sciences, 19*(8), 1723–1735.
98. Varela-Ortega, C., et al. (2016). How can irrigated agriculture adapt to climate change? Insights from the Guadiana Basin in Spain. *Regional Environmental Change, 16,* 59–70.
99. Vermeulen, S. J., Dinesh, D., Howden, S. M., Cramer, L., & Thornton, P. K. (2018). Transformation in practice: a review of empirical cases of transformational adaptation in agriculture under climate change. *Frontiers in Sustainable Food Systems, 2,* 65.
100. Iglesias, A., & Garrote, L. (2015). Adaptation strategies for agricultural water management under climate change in Europe. *Agricultural Water Management, 155,* 113–124.
101. Vano, J. A., et al. (2010). Climate change impacts on water management and irrigated agriculture in the Yakima River Basin, Washington, USA. *Climate Change, 102*(1–2), 287–317.
102. Hallegate, S. (2009). Strategies to adapt to an uncertain climate change. *Global Environmental Change, 19,* 240–247.
103. Taoyuan, W., Tianyi, Z., Karianne, B., Solveig, G., & Qinghua, S. (2016). Extreme weather impacts on maize yield: the case of Shanxi Province in China. *Sustainability-Basel, 9*(1), 41.
104. Hong, X., Tracy, T., & Evan, G. (2016). Climate change and maize yield in Iowa. *PLoS ONE, 11,* e0156083.
105. Sordo-Ward, A., Granados, A., Iglesias, A., Garrote, L., & Bejarano, M. D. (2019). Adaptation effort and performance of water management strategies to face climate change impacts in six representative basins of Southern Europe. *Water, 11,* 1078.
106. Teutschbein, C., & Seibert, J. (2010). Regional climate models for hydrological impact studies at the catchment scale: a review of recent modeling strategies. *Geography Compass, 4*(7), 834–860.
107. Skoulikaris, Ch., Ganoulis, J., Tolika, K., Anagnostopoulou, Ch., & Velikou, K. (2017). Assessment of agriculture reclamation projects with the use of regional climate models. *Water Utility Journal, 16,* 7–16.
108. Teutschbein, C., & Seibert, J. (2012). Bias correction of regional climate model simulations for hydrological climate-change impact studies: review and evaluation of different methods. *Journal of Hydrology, 456–457,* 12–29.
109. Diaz-Nieto, J., & Wilby, R. L. (2005). A comparison of statistical downscaling and climate change factor methods: impacts on low flows in the River Thames United Kingdom. *Climatic Change, 69*(2–3), 245–268.
110. Fayaed, S. S., et al. (2019). Improving dam and reservoir operation rules using stochastic dynamic programming and artificial neural network integration model. *Sustainability-Basel, 11*(19), 5367.